Environmental Science Advances

ROYAL SOCIETY OF CHEMISTRY

PAPER

View Article Online
View Journal | View Issue

Cite this: *Environ. Sci.: Adv.*, 2022, **1**, 827

Engineering GO@Zn–Hap@CA porous heterostructure for ultra-fast and ultra-high adsorption efficacy: investigation towards the remediation of chromium and lead†

Monika Mahmud,[a] Md. Sahadat Hossain,[a] Mashrafi Bin Mobarak,[a] Md. Saiful Quddus,[a] Muhammad Shahriar Bashar,[b] Umme Sarmeen Akhtar,[a] Shirin Akter Jahan,[a] Dipa Islam[c] and Samina Ahmed *[ad]

In the contemporary era, research into the structures involving emerging 2D materials, inorganic components, and polymers has evolved at a tremendous pace for environmental protection and sustainability. Herein, this study reports the design and fabrication of a GO@Zn–Hap@CA porous heterostructured adsorbent using 2D graphene oxide (GO), inorganic zinc-doped hydroxyapatite (Zn–Hap) and cellulose acetate (CA) *via* a crosslinking approach for the removal of Cr(VI) and Pb(II) ions. The synthesized raw material and the developed heterostructured adsorbent were intensely characterized by X-ray diffraction (XRD), Fourier transform infrared (FT-IR) spectroscopy, X-ray photoelectron spectroscopy (XPS), atomic force microscopy (AFM), field emission scanning electron microscopy (FE-SEM), and N_2 gas adsorption–desorption analysis. The fabricated GO@Zn–Hap@CA heterostructure exhibited high roughness, high surface area and mesoporous texture and thereby has shown an enhanced capture of Cr(VI) and Pb(II) ions. Importantly, it possessed an ultrahigh maximum adsorption capacity of 384 mg g^{-1} and 400 mg g^{-1} for Cr(VI) and Pb(II) at pH = 2 and pH = 5, respectively. Investigation of the adsorption isotherm and kinetics indicate that both Cr(VI) and Pb(II) adsorption fitted well with the Freundlich isotherm model and pseudo-second-order kinetic model. While probing the kinetics, the equilibrium was observed to reach at an ultrafast duration, for instance, 50 min for chromium and 60 min for lead. A study on the effect of the co-existing ions revealed that the cations and anions had a less significant effect on Cr(VI) and Pb(II) adsorption. Such results offer insights into the intriguing potential of GO@Zn–Hap@CA for the elimination of hazardous pollutants from the aquatic environment.

Received 22nd June 2022
Accepted 29th September 2022

DOI: 10.1039/d2va00142j

rsc.li/esadvances

Environmental significance

Toxic heavy metal pollution in the aqueous environment due to rapid industrialization has indicated a burning global concern. The continuous use and intake of such polluted water can cause fatal health issues to the living beings. Herein, the study focuses on designing a porous structure *via* crosslinking strategy by employing two-dimensional graphene oxide, Zn doped hydroxyapatite and cellulose acetate for the eradication of chromium and lead from aqueous media. The engineered porous structure with high roughness and surface area facilitates efficient trapping of chromium and lead at ultrafast duration. The developed composite membrane also discloses excellent reusable potency of up to three cycles thereby promoting environmental sustainability.

1 Introduction

Designing structures with emerging materials for the decontamination of wastewater has been extensively intensified worldwide in the current industrial era. In industrial discharge, heavy metal ions (HMIs), Cr(VI), and Pb(II) are hazardous to aquatic life as well as human beings.[1,2] Beyond doubt, both Cr(VI) and Pb(II) lead to various persistent diseases, such as anemia, cancer, renal failure, lung obstruction, and liver damage.[3,4] Hence, the World Health Organization (WHO) set

[a]*Institute of Glass and Ceramic Research and Testing (IGCRT), Bangladesh Council of Scientific and Industrial Research (BCSIR), Dr Qudrat-i-Khuda Road, Dhanmondi, Dhaka-1205, Bangladesh. E-mail: shanta_samina@yahoo.com; Fax: +88-02-8613022; Tel: +88-1817549816*

[b]*IFRD, Bangladesh Council of Scientific and Industrial Research (BCSIR), Dr Qudrat-i-Khuda Road, Dhanmondi, Dhaka-1205, Bangladesh*

[c]*BTRI, Bangladesh Council of Scientific and Industrial Research (BCSIR), Dr Qudrat-i-Khuda Road, Dhanmondi, Dhaka-1205, Bangladesh*

[d]*BCSIR Laboratories Dhaka, Bangladesh Council of Scientific and Industrial Research (BCSIR), Dr Qudrat -i-Khuda Road, Dhanmondi, Dhaka-1205, Bangladesh*

† Electronic supplementary information (ESI) available. See DOI: https://doi.org/10.1039/d2va00142j

Cr(VI) as a class-I human carcinogen and announced the maximum allowable limit of total Cr (Cr(III) + (VI)) to 50.0 μg L^{-1} in drinking water.[5,6] Moreover, the United States Environment Protection Agency (US-EPA) has specified the limit for Pb(II) as 15 μg L^{-1} and 100 μg L^{-1} in drinking water and water supporting aquatic life, respectively.[7]

To date, numerous trending technologies such as reverse osmosis, electrochemical treatment, and advanced oxidation processes (AOPs) employed in water treatment[8,9] are associated with the generation of secondary pollutants, high capital, and energy requirements.[10,11] Nevertheless, adsorption is advantageous owing to its efficacy, simplicity, and cost-effectiveness.[12–14] Intrinsically, the adsorption capacity of the adsorbent exceedingly depends on the specific surface area (SSA), polarity, porous structure, and surface functional groups attached to the adsorbent surface.[14] Currently, various adsorbents, including inorganic materials,[15] double-layered hydroxides,[16] metal–organic frameworks,[17] 2D carbon-based materials,[18] and polymers[19] have drawn considerable attention.

Since 2004, the discovery of graphene[20] has received priority over other adsorbents in water treatment and sustainability by using its functionalized derivative. Specifically, graphene oxide (GO), a perfect 2D substance, holds a honeycomb lattice produced from the oxidation of inexpensive graphite.[21] The fundamental reason behind its priority is its two extraordinary features: (i) large surface area (theoretically 2630 m^2 g^{-1}),[22] which aids it in offering a suitable specific area for adsorption; (ii) great extents of epoxy, hydroxyl, and carboxyl functional groups on the basal planes and edges can easily fit with metal ions through the chelation mechanism or electrostatic interaction.[23,24] Therefore, in this research, graphene oxide is chosen for the adsorption of HMIs. Despite all of the unique properties of GO, there is a striking problem in that the solid GO sorbent tends to aggregate during adsorption due to π–π interactions and hence retard the adsorption phenomenon.[19,25,26] To solve this problem, composites of GO with different synthetic polymers as the support have been studied to fabricate mixed matrix membranes (MMMs).[25] Unfortunately, unbounded GO in the membrane creates electrostatic repulsion between negatively charged GO flakes, thereby causing instability in water.[27] Hence, GO membranes can also be stabilized through electrostatic interaction using multivalent cationic metals, polymer and crosslinking agents.[28] Therefore, to design a stable adsorbent, here GO is crosslinked with cellulose acetate (CA). The literature has also reported different works on GO composite membranes, for example, chitosan–GO,[29] GO–cellulose,[30] and GO–polyethyleneamine.[31]

Hydroxyapatite $Ca_{10}(PO_4)_6(OH)_2$, with abundant hydroxyl groups and minor water solubility, is recognized as a worthy material in wastewater treatment.[32,33] However, metal-doped hydroxyapatite has been reported to have high efficiency in water purification because of its small crystallite size and bulky surface area.[34,35] The structural flexibility of Hap allows for ion exchange in divergent crystallographic locations, but the core structure of HAP is left unchanged.[36] Hence, in this study, Zn-doped Hap was selected for the adsorbent constituent and was successfully synthesized to remove HMIs from an aqueous solution. Several works, such as Sn–Hap[35] for chromium and Mg–Hap[34] for lead removal, have been published.

Notably, cellulose acetate (CA), a bio-based polymer, is regarded as a polymer matrix membrane due to its better film-forming ability, biocompatibility, and eco-friendliness.[37] However, the CA film alone has poor mechanical and thermal properties. To overcome this weakness, CA is used with various materials like carbon nanotubes (CNTs)[38] and graphene oxide (GO).[39] As a consequence, CA is selected as a crosslinking polymer for the fabrication of the adsorbent.

In this research, we aim to engineer a new heterostructure containing these superior GO, Zn–Hap, and CA. Herein, the heterostructure is developed in a membrane form to overcome the aggregation of powder materials. A comprehensive study of the new heterostructure was employed by XPS to focus on the interaction and crosslinking within the materials. Importantly, the surface roughness has been measured by AFM and the surface area has been reported by performing N_2 gas adoption desorption analysis. Exclusively, the adsorption isotherms and kinetic models were studied to understand the mechanism of HMIs adsorption. Aside from this analysis, the effects of coexisting ions and the reusability of the heterostructure in different cycles are profoundly taken into account. Concisely, the overall goal of the research is to: (1) design a promising porous heterostructure and elucidate the interaction between GO, Zn–Hap and CA; (2) determine the adsorption parameters; (3) underline the remediation mechanism of the Cr(VI) and Pb(II) ions from aqueous solution.

2 Experimental

2.1 Materials

All chemicals utilized in this research include graphite powder (C, 200 mesh, 99.9999%, Alfa Aesar), sulfuric acid (H_2SO_4, 95–97%, Sigma Aldrich), potassium permanganate ($KMnO_4$, 99.0%, Sigma Aldrich), hydrogen peroxide (H_2O_2, 35%, Alfa Aesar), phosphoric acid, (H_3PO_4, Sigma Aldrich), hydrochloric acid (HCl, 38%, Sigma Aldrich), calcium hydroxide ($Ca(OH)_2$, Sigma Aldrich), zinc nitrate ($Zn(NO_3)_2 \cdot 6H_2O$, Fluka, 98%), EDTA (Sigma Aldrich, 99.4%), ammonia (NH_3) (Merck, Germany), and cellulose acetate (Sigma Aldrich; Mn 50 000 GP). Each material holds high purity, and was hence used without any prior treatment.

2.2 Methods

2.2.1 Preparation of graphene oxide. In this work, modified Hummer's method was followed to synthesize graphene oxide (GO).[40,41] Here, sulfuric acid (H_2SO_4) and phosphoric acid (H_3PO_4) were mixed in a volume ratio of 9 : 1, and stirred for quite a few minutes. Next, 0.225 g of graphite powder was added gradually, followed by the addition of 1.32 g of potassium permanganate ($KMnO_4$) into the solution mixture. After that, the solution was left for 6 h stirring until the solution turned into a dark greenish color. To remove excess $KMnO_4$, hydrogen peroxide (H_2O_2), 0.675 mL was added dropwise with stirring. Since the reaction is exothermic, it was subjected to cooling

with the support of an ice bath. The final solution was then washed with hydrochloric acid (HCl) and deionized water (DIW), and centrifuged at 5000 rpm. Lastly, the washed GO was oven-dried at 40 °C for 24 h to form the powder GO.

2.2.2 Preparation of Zn doped hydroxyapatite. Zn–Hap was synthesized by the sol–gel method. In that process, firstly, calcium hydroxide was dissolved in 50 mL of distilled water, followed by the mixing of zinc nitrate hexahydrate dissolved in 10 mL of distilled water. Meanwhile, the solution was continuously stirred for about 1 h at room temperature. Afterward, 0.033 mol of EDTA was added to 50 mL of deionized water, and deprotonated with the aid of conc. NH_3. Here, the (Ca + Zn)/P molar ratio at 1.67 was maintained. Then, it was stirred again for an additional 1 h, and H_3PO_4 was added to the mixture dropwise. Importantly, to maintain the pH at ~11 in the solution, concentrated ammonia was added dropwise. The subsequent solution was stirred overnight at 70–80 °C until the solvent was utterly evaporated. The ensuing gels were then oven-dried at 110 °C for ~10 h, followed by heating for 5 h at 900 °C in a furnace (heating rate was 1 °C min^{-1}).

2.2.3 Preparation of the GO@Zn–Hap@CA heterostructure. Firstly, GO and Zn–Hap in acetone were mixed in 50 : 50 ratios. Then, the mixture was extensively mixed at 5000 rpm for 2 h using a homogenizer (HG-15D). Afterward, 5% cellulose acetate was added and mixed at 5000 rpm for 1 h. Finally, the resultant solution was cast on a Petri glass of 60 mm in diameter. Then, the membranes were immerged in a water bath for the solvent inversion process to get the heterostructured GO@Zn–Hap@CA. Similarly, 5% cellulose acetate membrane was also prepared for comparison. Scheme 1 portrays the preparation of GO, Zn–HAP, and the fabrication of the GO@Zn–Hap@CA composite membranes.

2.3 Instrumental characterization

2.3.1 XRD analysis. An X-ray diffractometer (PANalyticalX'Pert PRO PW 3040) was used to determine the crystallinity of the samples. The data were recorded by nonstop scanning with 0.01 steps and 2θ = 5–80° using Cu Kα (λ = 1.54060 Å) radiation. The Cu tube was operated at a voltage of 40 kV and current of 30 mA, and the chiller temperature was maintained at 19–20 °C.

2.3.2 XPS analysis. An X-ray photoelectron spectrometer (K-Alpha) was employed to evaluate the chemical composition of the films. The initial survey and core-level spectra were attainted with the aid of an Al K-Alpha monochromatic X-ray source (1486.69 eV) operated at 15 kV and 10 mA. The residual pressure of the analysis chamber was kept below 10^{-8} torr. The core level C 1s, O 1s, Ca 2p, P 2p, Zn 2p spectra, after background subtraction, were subjected to curve-resolving by applying a Gaussian line shape, along with a Lorentzian broadening function.

2.3.3 N_2 adsorption isotherms at 196 °C. To determine the textural characteristics of GO, Zn–Hap, CA membrane, and GO@Zn–Hap@CA composite membranes, nitrogen adsorption–desorption isotherms were accomplished at 196 °C using BET-201-A. The Brunauer–Emmett–Teller (BET) model[42,43] was used to estimate the specific surface area, while the data range of P/P_0 was taken between 0.05–0.35. Additionally, the Barrett–Joyner–Halenda (BJH) model[44] was used to evaluate the sample pore size and pore volume.

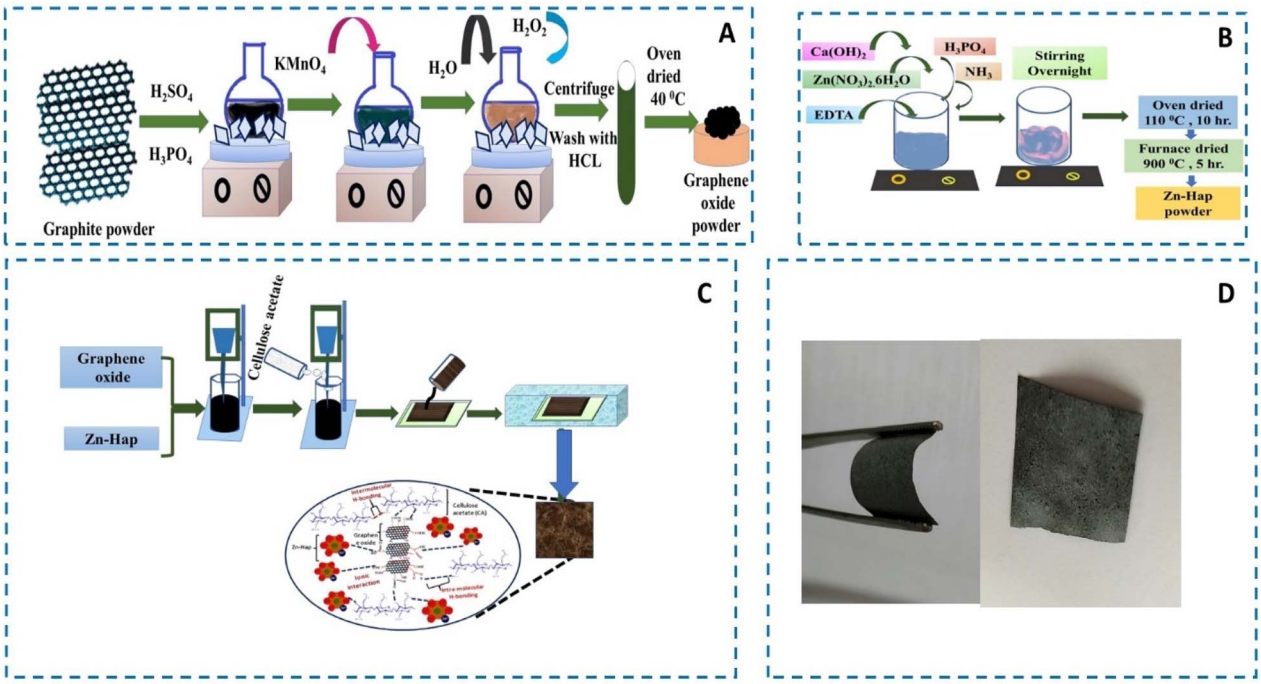

Scheme 1 Synthesis of GO (A); synthesis of Zn–Hap (B); preparation of GO@Zn–Hap@CA composite membrane (C); digital photograph of GO@Zn–Hap@CA (D).

2.3.4 FT-IR spectroscopy. The samples functional groups were identified using FT-IR comprising the attenuated total reflectance (ATR) facility (IR-Prestige 21, Shimadzu Corporation, Japan). The spectra were recorded in the 4000–400 cm^{-1} wavenumber range with the spectral resolution at 4 cm^{-1}.

2.3.5 Morphological analysis. The synthesized sample and developed composite morphology were examined by scanning electron microscope, SEM (PHENOM PRO) and field emission scanning electron microscope, FESEM (JSM-7610F) at an accelerating voltage of 5.0 kV. Samples are sputter-coated with platinum before testing.

The topography and surface roughness of CA and GO@Zn–Hap@CA composite membrane were attained by atomic force microscopy (Flex AFM, C3000, Nanosurf, Switzerland) without any preparation of samples. The sample of the surface area (5 × 5 mm) was placed on a holder. The sample was subjected to an oscillating cantilever tip sinusoidally with 350 kHz resonating frequency. The mean surface roughness of the membrane was calculated by the following equation:[45]

$$R_a = \frac{1}{L_x L_y}\int_0^{l_x}\int_0^{l_y} |f(x,y)|\mathrm{d}x\mathrm{d}y \quad (1)$$

Here, $f(x, y)$ is the surface relative to the center of the plane, and L_x and L_y represent the surface dimensions in the x and y directions, respectively. Consequently, the root means square (R_q) values were derived from the AFM images, which were calculated from the average of the values measured in random R_q values using the following equation.[45]

$$R_q = \left[\left(\frac{1}{L}\right)\int_{l_y}^{l_x}\int_{l_y}^{l_x} Z^2(x,y)\mathrm{d}x\mathrm{d}y\right]^{1/2} \quad (2)$$

Here, l_x and l_y are the evaluation length, and Z is the profile height functions.

2.3.6 Batch adsorption analysis. The experiments were carried out at different parameters, such as pH value,[2–8] contact time (5–100 min), adsorbent dosage (0.05–1 g L^{-1}), and initial Cr(VI) and Pb(II) ion concentration (30–500 mg L^{-1}). For the adsorption test, the required amounts of the potassium dichromate and lead nitrate were taken to prepare a 1000 ppm stock solution. Then, the concentrations (30–500 mg L^{-1}) of the volume (75 mL) of each metal ion were prepared. After that, the pH value of the sample solution was attuned with the aid of NaOH and HCl. Subsequently, the GO@Zn–Hap@CA composite membrane was added to the solution at a specific dosage. Throughout the study, the shaking speed was set to 220 rpm. The concentration of the Cr(VI) ion and Pb(II) ion was analyzed by atomic absorption spectrometer, AAS (Analytic Jena, NOVAA 350) using an acetylene-air flame.

2.3.7 Isotherm and kinetics study. The isotherm study is imperative for designing the science of adsorption phenomenon as the adsorption isotherm profoundly illustrates how the adsorbent surface and the pollutants interact. In this study, the Langmuir, Freundlich, Temkin and Dubinin–Radushkevich (Dub–Rad) isotherm models have been applied to explore the purging potency of the heavy metal ions. Linear and non-linear Langmuir isotherms are represented by the following eqn (3) and (4) respectively.[46]

$$\frac{C_e}{q_e} = \frac{1}{K_L q_m} + \frac{C_e}{q_m} \quad (3)$$

$$q_e = \frac{q_m k_L C_e}{1 + K_L C_e} \quad (4)$$

Here, q_e (mg g^{-1}) is the experimental adsorption capacity, C_e (mg L^{-1}) is the equilibrium concentration of HMIs in solution, q_m (mg g^{-1}) is the maximum adsorption capacity, and K_L (L mg^{-1}) denotes the Langmuir constant that represents the binding power (*i.e.*, adsorptive strength) between the adsorbent and adsorbates.

Linear and non-linear Freundlich isotherms are addressed by the following eqn (5) and (6), respectively.[47]

$$\ln q_e = \ln K_f + \frac{1}{n}\ln C_e \quad (5)$$

$$q_e = K_f C_e^{1/n} \quad (6)$$

Here, K_f (mg g^{-1}) is the Freundlich isotherm constant and is associated to the relative adsorption capacity of the adsorbent, and n is a constant signifying the adsorption intensity.

The linear and non-linear D–R isotherms are represented by the following eqn (7) and (8) respectively.[48]

$$\ln Q_e = \ln Q_m - K_{DR}\epsilon^2 \quad (7)$$

$$Q_e = Q_m e^{k_{DR}\varepsilon^2} \quad (8)$$

Here, Q_m (mg g^{-1}) means the D–R maximum adsorption capacity, K_{DR} (mol^2/Kj^2) denotes the mean adsorption energy and ε^2 (J mol^{-1}) is the Polanyi potential. The e is estimated using the equation below:

$$\epsilon = RT\ln(1 + 1/C_e) \quad (9)$$

where R, T, and C_e characterize the gas constant (8.31 J mol^{-1} k^{-1}), absolute temperature and equilibrium concentration of the adsorbate, respectively.

Linear and non-linear Temkin isotherms are represented by the following eqn (10) and (11) respectively.[49]

$$q_e = A\ln K_T + A\ln C_e \quad (10)$$

$$q_e = A\ln(K_T C_e) \quad (11)$$

$$A = \frac{RT}{b} \quad (12)$$

Here, A (unitless) is correlated to the Temkin isotherm constant; b (J mol^{-1}) denotes the heat of adsorption; K_T (L g^{-1}) presents the Temkin equilibrium binding constant; and R and T are the gas constant (8.31 J mol^{-1} K^{-1}) and temperature, respectively.

The kinetics of adsorption of Cr(VI) and Pb(II) on GO@Zn–Hap@CA were assessed with the pseudo-first order, pseudo-second order, and Elovich model by fitting the experimental data. The linear and non-linear pseudo-first-order Lagergren

equations are given by the following eqn (13) and (14) respectively.[50]

$$\log(q_e - q_t) = \log q_e \frac{k_1}{2.203} t \quad (13)$$

$$q_t = q_e(1-e^{-k_1 t}) \quad (14)$$

Here, k_1 is the pseudo-first-order rate constant (min^{-1}), and q_e and q_t are the amounts of HMIs ions adsorbed (mg g^{-1}) at equilibrium and at time t (minutes), respectively.

The linear and non-linear pseudo-second-order models can be expressed as eqn (15) and (16) respectively:[51]

$$\frac{1}{q_t} = \frac{1}{k_2 q_e^2} + \frac{1}{q_e} \quad (15)$$

$$q_t = \frac{q_e^2 k_2 t}{1 + q_e k_2 t} \quad (16)$$

where k_2 (g mg^{-1} min^{-1}) is the rate constant of the pseudo-second order adsorption, q_e (mg g^{-1}) is the amounts of HMIs ions adsorbed at equilibrium, and q_t (mg g^{-1}) describes the adsorption capacity at time t.

The linear and non-linear forms of the Elovich kinetics model are represented by the following eqn (17) and (18) respectively.[52]

$$q_t = \frac{1}{\beta}\ln(\alpha\beta) + \frac{1}{\beta}\ln(t) \quad (17)$$

$$q_t = \frac{1}{\beta}\ln(1 + \alpha\beta t) \quad (18)$$

where, q_t (mg g^{-1}) defines the adsorption capacity at time t, a (mg g^{-1} min^{-1}) denotes the rate of chemisorption at zero coverage, and $ß$ (g mg^{-1}) defines the maximum coverage of the surface of the adsorbate.

2.3.8 Regeneration study. Regeneration of the exhausted GO@Zn–Hap@CA was carried out using NaOH (0.1 M and 0.5 M) and HCl (0.1 M and 0.5 M) to remove the adsorbed Cr(VI) Pb(II), respectively. The GO@Zn–Hap@CA after Cr(VI) and Pb(II) adsorption was collected for treatment with NaOH and HCl at 220 rpm for 30 minutes, followed by careful washing with DI water to achieve neutral pH. A reusability study for multi-cycle Cr(VI) and Pb(II) adsorption was investigated with the newly regenerated GO@Zn–Hap@CA in freshly prepared Cr(VI) and Pb(II) solutions at the optimized parameter. After adsorption, the used GO@Zn–Hap@CA composite membrane was taken out from the solution, and the corresponding concentration was measured by AAS. Meanwhile, the exhausted GO@Zn–Hap@CA was regenerated using the same protocol for the next cycle. Three successive adsorption–desorption cycles were examined with the regenerated GO@Zn–Hap@CA composite membrane.

3 Results and discussion

3.1 XRD and FTIR analysis

Fig. 1a displays the XRD patterns of Zn–Hap, GO, CA and GO@Zn–Hap@CA membranes. The XRD spectra of the Zn-doped Hap resemble the unique phase of hexagonal hydroxyapatite (Space group $P6_3$/standard card ICDD-PDF number 9-432).[53] Here, the main apatite phase, $2\theta = 31.87°$ (211 plane), confirmed the synthesis of Zn–Hap.[54] The diffraction pattern of GO exhibits a peak at $2\theta = 10.3°$ of plane (001) and interlayer distance, $d = 0.86$ nm, which arises mainly due to the oxidation of graphite.[41] The characteristic peaks of CA at $2\theta = 15.06°$ and 17.34° could be assigned to a semi-crystalline structure, while the peak at $2\theta = 22.2°$ refers to the amorphous phase.[55] In GO@Zn–Hap@CA, all of the dominating peaks of GO and Zn–Hap are observed. However, the spectra of amorphous CA were suppressed by the well-crystallized phase of Zn–Hap and GO.

FTIR spectroscopy was further employed to interpret the functionality of the as-prepared GO, Zn–Hap, CA and GO@Zn-Hao@CA. In the spectrum of GO in Fig. 1b, the appearance of a major peak at 3400 cm^{-1} confirms the symmetric stretching vibration of –OH of the surface carbocyclic ring.[54] Other various oxygenated bond vibrational features at 1729 cm^{-1} and 1053 cm^{-1} could be attributed to the C═O and C–O (alkoxy) stretching vibrations, respectively,[55] verifying the richness of the oxygenated group. In Zn–Hap, the spectrum bands at 562–564 cm^{-1} were ascribed to the O–P–O bending mode (ν_4). Meanwhile, those within the 1036 and 1048 cm^{-1} regions are linked to the asymmetric stretching mode of PO_4^{3-} (ν_3).[53,56] Normally, the adsorbed water molecules in Zn–Hap are defined by the vibrational bands from 3000–3800 cm^{-1}. In the CA spectrum, the peaks at 1760 cm^{-1}, 1242 cm^{-1}, and 1400 cm^{-1} are ascribed to the –COO–, CO, and CH bonds, respectively. Moreover, the peak at 1053 cm^{-1} is assigned to the deformation vibrations of the CH and OH groups, and the features at 903 cm^{-1} are ascribed to the deformation vibrations of the –COC–, –CCO– and –CCH groups.[1] In the spectrum of GO@Zn-Hao@CA, major peaks appeared at 1739 cm^{-1}, 1221 cm^{-1}, 1032 cm^{-1}, and 573 cm^{-1}, which correspond to the –COO–, C–O (epoxy), C–O (alkoxy), and O–P–O bonds, respectively. Here, a slight shifting in the peak position is observed compared to those of the characteristics peaks of Zn–Hap, GO, and CA. These might be because of the H-bonding interaction of CA, GO and Zn–Hap within the functional sites of GO@Zn-Hao@CA. Therefore, the FTIR results disclose the crosslinking interaction of CA with GO and Zn–Hap by peak shifting.

3.2 XPS analysis

XPS was performed to observe the elemental compositions and oxidation states of the as-prepared Zn–Hap, GO, CA and GO@Zn–Hap@CA membranes. As shown in Fig. 2, the C, O, Ca, P, and Zn elements were found on the survey XPS spectra of GO@Zn–Hap@CA, indicating that the composite was fully developed.

In the XPS survey spectra of the GO and CA, the percentage of C 1s was recorded at 61.8% and 62.3%, respectively. In sharp contrast, the carbon content in the GO@Zn–Hap@CA composite was significantly increased to 79.41%, verifying the addition of carbon-containing GO and CA.

The core level C 1s spectra of GO (Fig. 3a) were fitted into peaks at 284.8 eV, 286.9 eV and 288.7 eV, which corresponded to

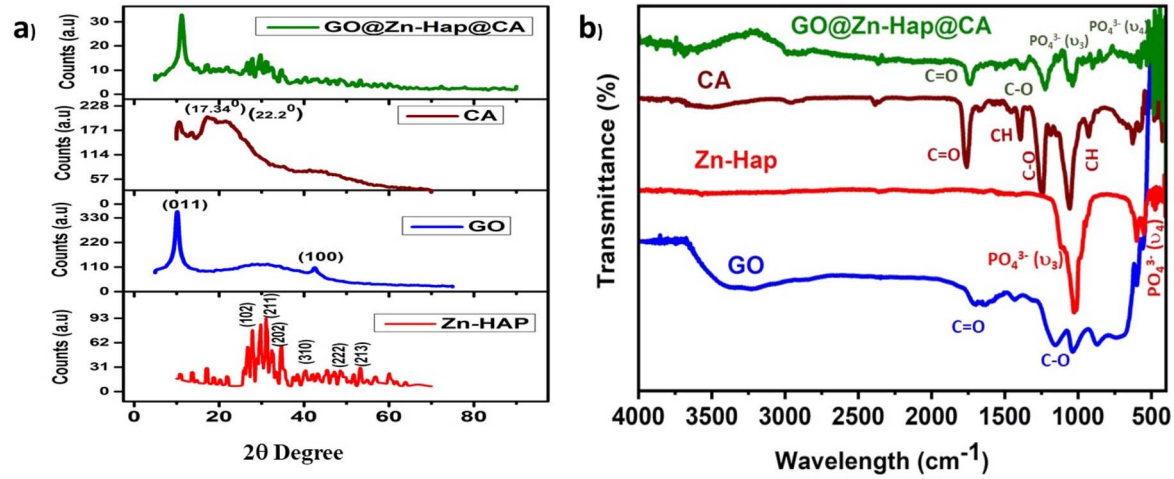

Fig. 1 (a) XRD pattern of Zn–Hap, GO, CA, and GO@Zn–Hap@CA; (b) FTIR analysis of GO, Zn–Hap, CA, and GO@Zn–Hap@CA.

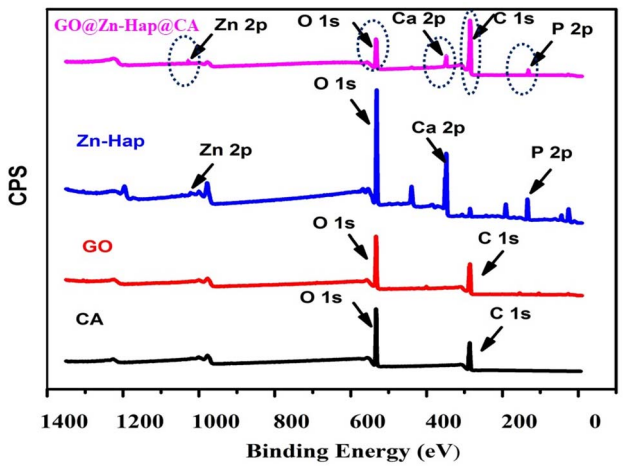

Fig. 2 XPS survey spectrum of the cellulose acetate (CA) membrane, graphene oxide (GO), Zn–Hap and GO@Zn–Hap@CA.

the C–C/C=C, O–C–O and O–C=O bonds.[57] Furthermore, The C 1s of CA (Fig. 3b) were deconvoluted into five peaks centered at 285.1 eV, 285.6 eV, 286.8 eV, and 287.8 eV assigned to C–C, C–H, O–C–O, and O–C=O, respectively.[58] However, in GO@Zn–Hap@CA (Fig. 3c), the assigned positions of the C–C/C–H, C–OH, C–O, and O–C=O functional groups were shifted and found at binding energies of 284.7 eV, 285.7 eV, 287 eV, and 289.3 eV, respectively.

Additionally, the relative intensity of C–C was observed to increase, whereas the intensities of O–C=O and C–O decreased compared to GO and CA. This finding reveals the strong interaction of the carboxyl and carbonyl groups from GO and CA in the developed GO@Zn–Hap@CA.

Fig. 3d exhibits the deconvoluted O 1s spectra at 532.7 eV, 530.9 eV and 535 eV of GO, which belong to the C–O, C=O, and O–H groups.[44] For the O 1s spectra (Fig. 3e) of CA, the surface functional O–C, O=C, and O–H groups depict peaks at 531.5 eV, 530 eV, and 532 eV, while Zn–Hap shows a broad peak at 532.5 eV (Fig. 3f). Nevertheless, due to the interaction of the functional group in GO@Zn–Hap@CA, the C–O/O–H and O–C groups experienced peaks at 532.9 eV and 531.3 eV (Fig. 3g), respectively. The XPS peaks of Ca 2p in Zn–Hap appeared for the $2p_{3/2}$ and $2p_{1/2}$ electronic states of Ca(II) at 348.0 eV and 351.5 eV (Fig. 3h), respectively.[47] However, the spin–orbit for $2p_{3/2}$ and $2p_{1/2}$ observed a decrease in intensity and a blue shift at the peak positions of 347.7 eV and 351.2 eV in GO@Zn–Hap@CA (Fig. 3i), respectively. The binding energy of P 2p was detected at 133 eV both in Zn–Hap and GO@Zn–Hap@CA (Fig. 3j and k).

The XPS of Zn–HAp reveals that the Zn 2p spectrum (Fig. 3l) exhibits two peaks at 1022.2 eV and 1045 eV, confirming the Zn doping. Conferring to the research conducted by Zhang *et al.*,[59] these two peaks can be attributed to the $2p_{3/2}$ and $2p_{1/2}$ electronic states of Zn(II). However, only a peak at 1022.4 eV was observed in GO@Zn–Hap@CA (Fig. 3m).

These overall shifting of the peak intensity of the functional groups verify the crosslinking interaction *via* intramolecular and intermolecular H-bond within the molecules of the GO@Zn–Hap@CA.

3.3 Morphological analysis

Fig. 4a–c illustrates the SEM micrograph of Zn–Hap (a), GO (b), and CA (c). Zn–Hap displays spherical shapes, but in agglomerated order.[53] GO exhibits layered, crinkled and fairly wrinkled patterns.[40] The top view of the CA film portrays a smooth texture, where the cross-section shows the porous structure.[58]

The high-magnification FE-SEM image of GO@Zn–Hap@CA is shown in Fig. 4d. Spherical-sized Zn–Hap and GO layers are found on the top surface of the composite. Remarkably, the porous heterostructure is confirmed by the cross-section of the GO@Zn–Hap@CA (Fig. 4e), which clearly shows the pores within the heterostructure.

The surface topology and roughness of the CA membrane and GO@Zn–Hap@CA membranes were investigated by AFM. Fig. 4g demonstrates the 3D morphology of the CA membrane with high roughness and smooth areas owing to the spatial arrangement in the crystalline and amorphous zones. Here, the well-ordered crystalline alignment indicates high roughness areas with an

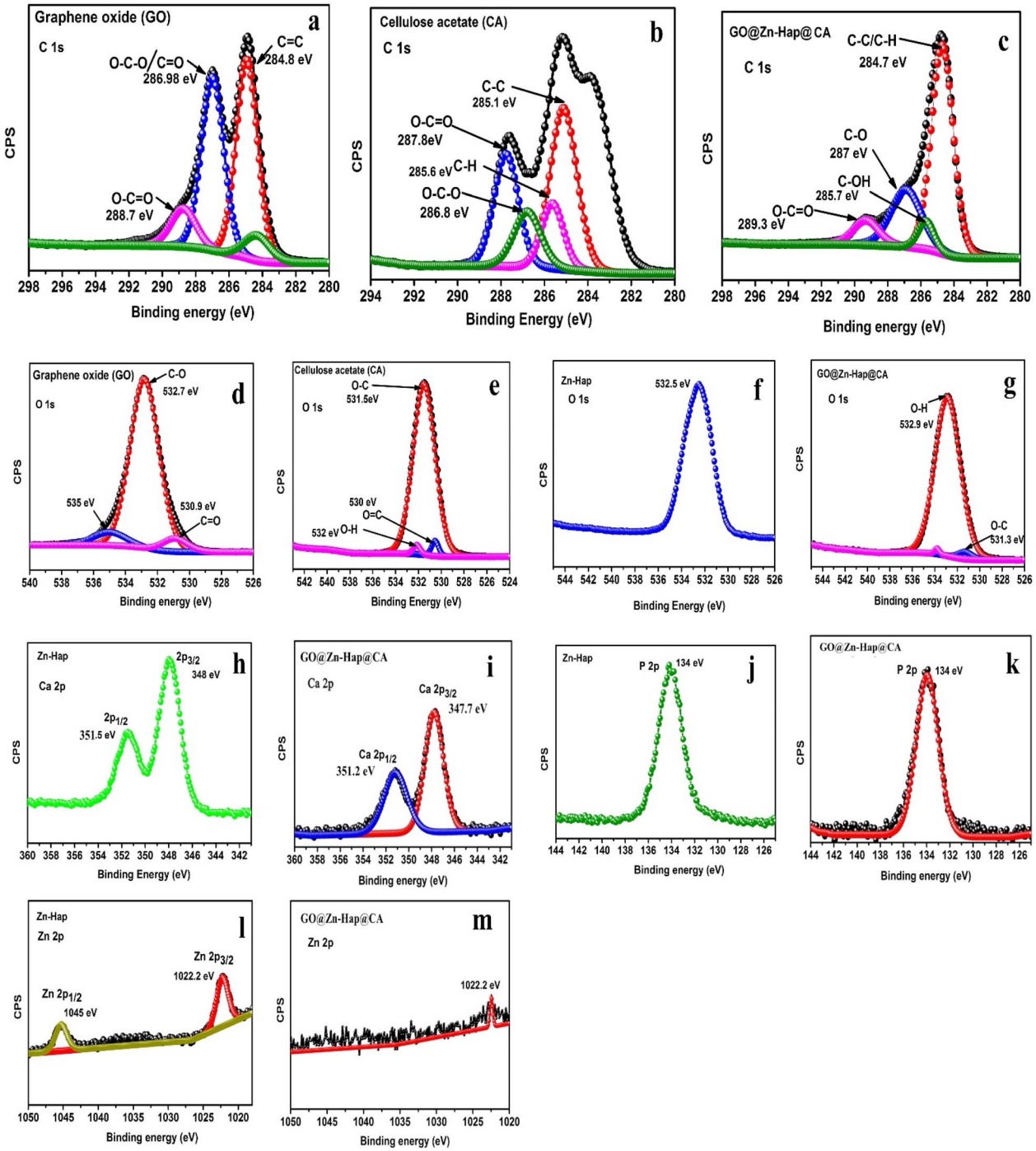

Fig. 3 XPS deconvoluted C 1s spectra of GO (a), CA (b) and GO@Zn–Hap@CA (c); O 1s spectra of GO (d), CA (e), Zn–Hap (f), GO@Zn–Hap@CA (g); Ca 2p spectra of Zn–Hap (h) and GO@Zn–Hap@CA (i); P 2p spectra of Zn–Hap (j) and GO@ Zn–Hap@CA (k); Zn 2p spectra of Zn–Hap (l) and GO@ Zn–Hap@CA (m).

average roughness (R_a) of about 68.8 nm and root mean square roughness (R_q) of about 111.11 nm. However, it was noticed that (Fig. 4i) the average roughness (R_a) was increased in GO@Zn–Hap@CA in comparison with the CA film from 68.8 to 137.6 nm. Additionally, a marked increment of the root mean square roughness (R_q) was observed from 111.11 nm in the CA film to 194.03 nm in the GO@Zn–Hap@CA composite. The increased R_q indicates the successful incorporation of Zn–Hap and GO. The peaks of roughness in GO@Zn–Hap@CA are considered as a hook to interlock guest molecules in aqueous environments.[55,60]

3.4 BET specific surface area measurements

The surface area and porosity play a significant role in determining the adsorbent performance.[61,62] Nitrogen gas adsorption–

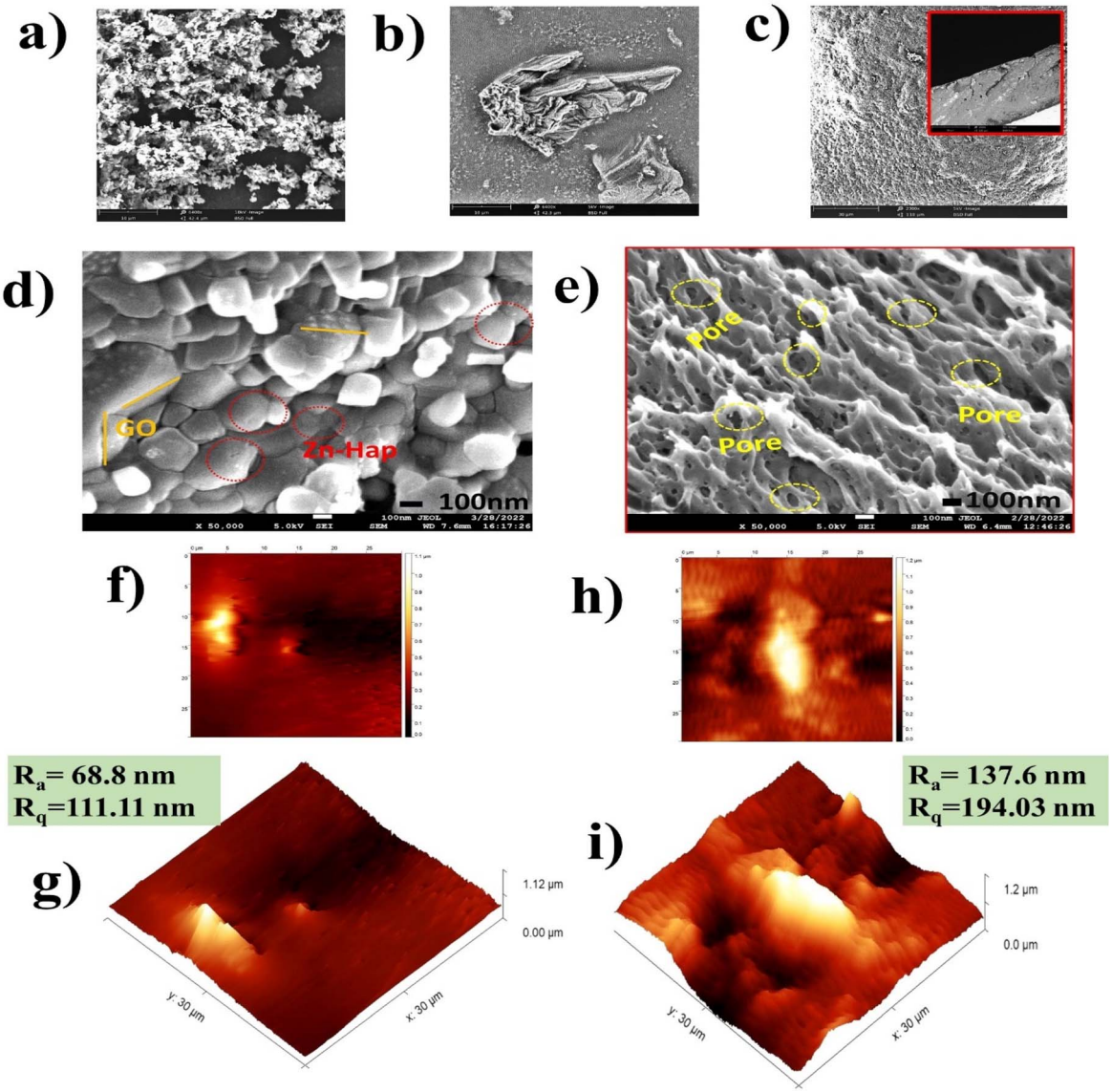

Fig. 4 SEM image of Zn–Hap (a), GO (b), CA membrane (c), and the CA membrane cross section (inset); FESEM image of the GO@Zn–Hap@CA membrane (d), FESEM image of the GO@Zn–Hap@CA membrane cross-section (e); AFM of the CA membrane 2D image (f) and 3D image (g); AFM of the GO@Zn–Hap@CA membrane 2D image (h) and 3D image (i).

desorption isotherms of the Zn–Hap, GO, CA and GO@Zn–Hap@CA composite membrane are shown in Fig. 5a. Table 1 summarizes the obtained BET surface area, pore-volume, and pore size diameter of the materials. The type of isotherms and pores were defined according to the IUPAC (International Union of Pure and Applied Chemistry) classification. According to IUPAC, the pore within the porous materials is signified as micropores (<2 nm in diameter), mesopores (2–50 nm), and macropores (>50 nm).[18] The results indicated that the Zn–Hap and GO exhibit Type IV isotherm with a H4 type hysteresis loop, whereas CA and GO@Zn–Hap@CA show isotherms of Type III with a H3 type hysteresis loop (P/P_0. range of 0.4 to 0.99).

The obtained BET surface area of the GO and Zn–Hap are 66 $m^2\ g^{-1}$ and 5 $m^2\ g^{-1}$, respectively. However, the BET surface area of the GO@Zn–Hap@CA composite was found to be 39 $m^2\ g^{-1}$, which is lower than that of GO, but considerably higher than those of Zn–Hap and CA (10 $m^2\ g^{-1}$). It is possible that CA was wrapped on GO, and resulted in the decrease in surface area of GO@Zn–Hap@CA compared to GO. Significantly, in the GO@Zn–Hap@CA composite membrane, the average pore diameter is reduced because the large pores of CA are filled with GO and Zn–Hap (Fig. 5b). Indeed, the obtained high surface area is exponentially beneficial for the adsorption of more heavy metals, and the mesoporous texture facilitates the diffusion of HMIs within the pores.

3.5.1 Effect of pH and adsorbent dosage. Since the solution pH extensively governs the speciation of the heavy metal ion species, and controls the protonation and deprotonation of the surface-active sites of the adsorbents, it is regarded as a crucial parameter in the adsorption of ionic pollutants. Fig. 6a displays

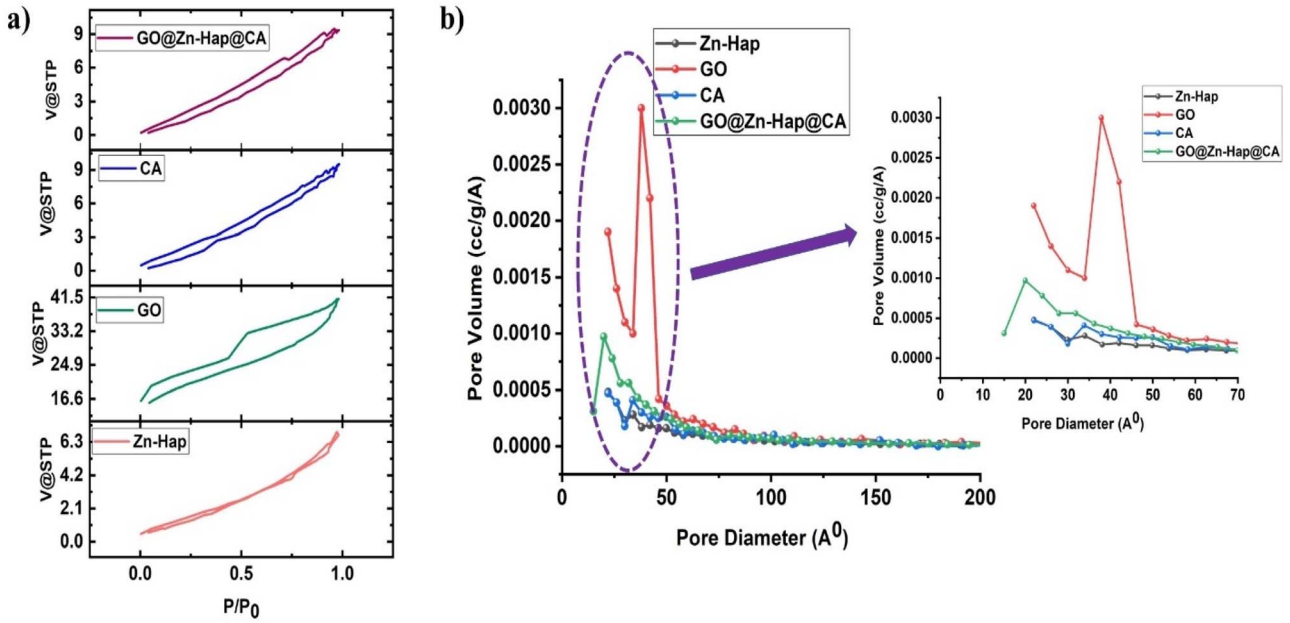

Fig. 5 (a) N_2 adsorption desorption isotherms, (b) BJH adsorption pore size distribution for GO, Zn–Hap, CA membrane and GO@Zn–Hap@CA.

Table 1 BET surface area, pore volume, and average pore size diameter of the as-synthesized GO, Zn–Hap, CA membrane and GO@Zn–Hap@CA nanocomposite membrane

Materials	Specific area, BET ($m^2\ g^{-1}$)	Pore volume BJH ($cm^3\ g^{-1}$)	Average pore size diameter (nm)
GO	66	0.0634	3.8
Zn–Hap	5	0.0104	8.25
Cellulose acetate	10	0.0157	5.48
GO@Zn–Hap@CA	39	0.0144	4.52

the effect of pH on the Cr(VI) and Pb(II) adsorption. Another important parameter which affects the adsorption process is the point of zero charge (pH_{pzc}). Generally, at that point, the surface charges of the adsorbent are zero. Moreover, it is well known that the adsorbent surface is positively charged to pH < pH_{pzc} and negatively charged to pH > pH_{pzc}. From Fig. 6b, it is observed that the point of zero charge of the GO@Zn–Hap@CA composite membrane is 4.2.

Notably, chromium is found in the chromic acid (H_2CrO_4), hydrogen chromate ($HCrO_4^-$), chromate (CrO_4^{2-}), and dichromate ($Cr_2O_7^{2-}$) forms in aqueous solution. However, at pH < 1, H_2CrO_4 exists. Furthermore, at pH values between 1 to 6.5, $HCrO_4^-$ exists, while at pH > 6.5, CrO_4^{2-} forms.[63]

The following equations[64] represent the speciation of chromium at different pH values:

$$HCrO_4^- \leftrightarrow CrO_4^{2-} + H^+,\ pK_a = 5.9 \quad (19)$$

$$H_2CrO_4 \leftrightarrow HCrO_4^- + H^+,\ pK_a = -0.26 \quad (20)$$

$$Cr_2O_7^{2-} + H_2O \leftrightarrow 2HCrO_4^-,\ pK_a = 2.2 \quad (21)$$

The as-prepared GO@Zn–Hap@CA holds alkoxyl, carboxyl, hydroxyl, and phosphate groups, which are easily protonated in an acidic environment. Therefore, adsorption of $HCrO_4^-$ occurred *via* the electrostatic force of attraction between the positively charged GO@Zn–Hap@CA and the negatively charged $HCrO_4^-$. Nevertheless, with the gradual climb of solution pH, adsorption decreases owing to the infirm protonation, as well as electrostatic repulsion between the GO@Zn–Hap@CA composite surfaces and the negatively-charged pollutants. Meanwhile, precipitation of chromium metal occurs at pH > 6.0. Those results verify that the adsorption capacity of Cr(VI) by GO@Zn–Hap@CA is exceedingly reliant on the solution pH. Furthermore, the utmost adsorption capacity could be obtained at pH = 2.0. Thus, for the subsequent study, pH = 2.0 was selected as the optimum pH for Cr(VI) adsorption. Additionally, at pH = 2 (below pH_{pzc} = 4.2), the adsorbent surface is positively charged and fosters the adsorption of anionic chromate ions.

In the case of Pb(II) ions, at acidic pH, hydrogen ions in solution compete with the Pb(II) ions for adsorption sites. This results in the trivial adsorption capacity for Pb(II) ions.[65] With the increment of pH value, the carboxyl groups in the composite are converted to carboxylate anions.[65] Hence, the electrostatic attraction between the Pb(II) ions and GO@Zn–Hap@CA is improved, which facilitates the adsorption of Pb(II) ions. Moreover, the rising pH value initiates a high concentration of OH^- ions in solution, which tends to coordinate with Pb(II) ions to form a $Pb(OH)_2$ precipitate. With increasing pH beyond pH = 6, $PbOH^+$, Pb_2OH^{3+}, $Pb(OH)_2$, $Pb(OH)4^{2-}$ and $Pb(OH)^{3-}$ are found in the solution, while a white precipitate of $Pb(OH)_2$ is formed at pH 8.0.[66]

Therefore, according to the investigated results, pH 5.0 was verified as the optimum pH value for the adsorption of Pb(II) ions to avoid precipitation. Moreover, at pH = 5 (above pH_{pzc} = 4.2), the adsorbent surface possesses negative charges that increase the electrostatic attraction and strong adsorption of positive metal ions.

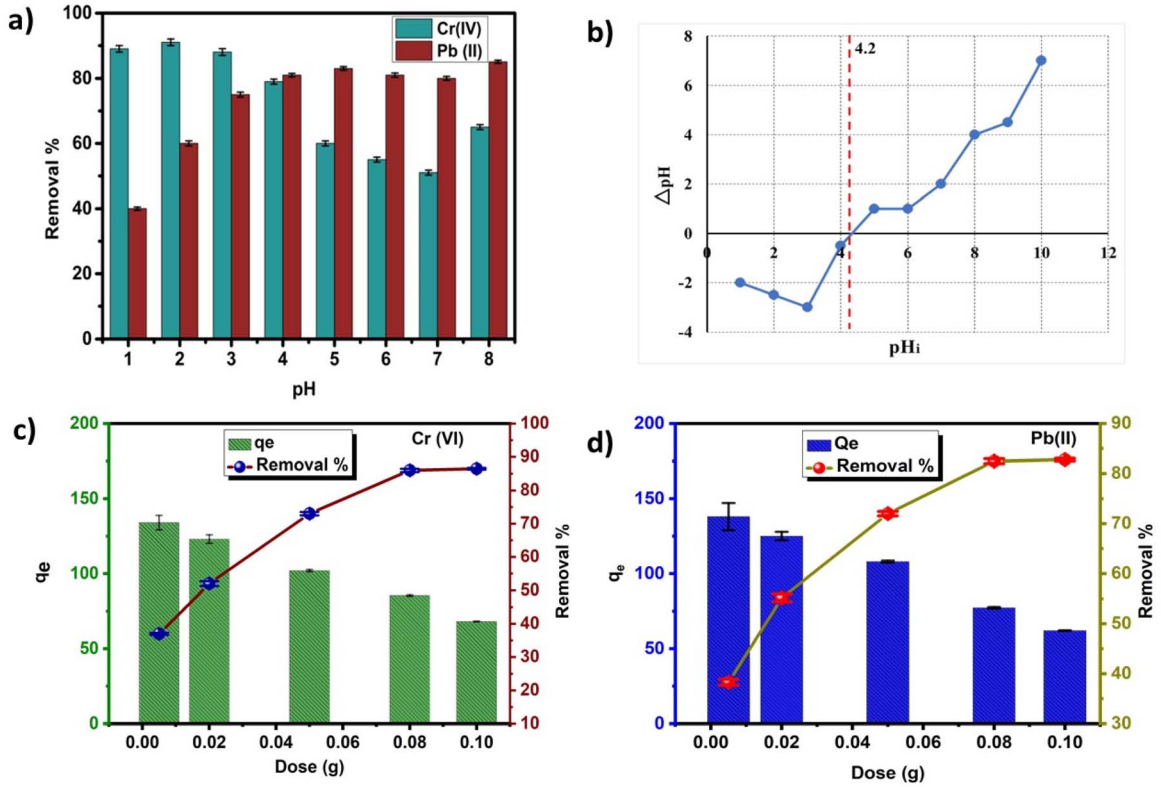

Fig. 6 (a) Effect of pH on Cr(VI) and Pb(II) adsorption (initial metal concentration 100 ppm, dose 0.05 g; contact time:100 minutes); (b) point of zero charge graph of GO@Zn–Hap@CA; (c) effect of dose on Cr(IV) adsorption; (d) effect of dose on Pb(II) adsorption (pH 2 = Cr(VI) and pH 5 = Pb(II), initial metal concentration of 100 ppm, contact time of 100 minutes).

The effect of the adsorbent dosage for Cr(VI) and Pb(II) removal in a fixed pollutant concentration (100 mg L^{-1}) was investigated, and the results are displayed in Fig. 6c and d. Here, it was found that for Cr(VI) and Pb(II), the percentage of removal increases from 37% to 73% and 40% to 72%, respectively, upon increasing the adsorbent dosage from 0.01 g to 0.1 g. For adsorbent dosages from 0.01 to 0.05 mg mL^{-1}, the removal efficiency increases, which implies that more active sites become available for adsorption of HMIs with the increasing amount of adsorbent. However, upon extending the dosages beyond 0.05 g, the removal percentage remains the same, which indicates the existence of more adsorbent than the fixed concentration of HMIs.[67,68]

3.5.2 Initial concentration effect and adsorption isotherm study. The influence of the initial Cr(VI) and Pb(II) concentration was explored on GO@Zn–Hap@CA Fig. 7(a and b), Zn–Hap (Fig. S1 and S2†), GO (Fig. S3 and S4†), and CA (Fig. S5 and S6†). Here, Cr(VI) and Pb(II) are adsorbed favorably on the GO@Zn–Hap@CA surface at pH 2 and pH 5, respectively. From Fig. 7(a and b), it is observed that the adsorption capacity of GO@Zn–Hap@CA is quickly enhanced by increasing the initial concentration of Cr(VI) and Pb(II) from 30 to 500 mg L^{-1}, suggesting that there are sufficient adsorption sites on the adsorbent.

An adsorption isothermal investigation was performed by linear and non-linear isothermal models, where the best suited model was determined by the regression co-efficient (R^2) value. Here, for the GO@Zn–Hap@CA composite, the regression coefficient (R^2) in the linear Langmuir and linear Freundlich isotherm are well-fitted compared to other linear isotherms for both Cr(VI) and Pb(II). However, the R^2 value in the linear Freundlich isotherm is close to ~1 compared to the linear Langmuir isotherm, indicating that the linear Freundlich isotherm is better fitted for Cr(VI) and Pb(II) adsorption. Fig. 7c and d shows the liner fitting Freundlich isotherm of Zn–Hap, GO, CA and GO@Zn–Hap@CA for Cr(VI) and Pb(II) adsorption. The plots of all other linear isotherms, including Langmuir, Temkin and Dubinin–Radushkevich (Dub–Rad) models, are provided in Fig S7 and S8.† The value of the parameters of the linear isotherms are shown in Table 2. Notably, the linear Langmuir adsorption capacities of Cr(VI) onto Zn–Hap, GO, CA, and GO@Zn–Hap@CA were 78 mg g^{-1}, 87 mg g^{-1}, 113 mg g^{-1}, and 384 mg g^{-1} at room temperature. For Pb(II), the linear Langmuir adsorption capacity onto Zn–Hap, GO, CA, and GO@Zn–Hap@CA were 86 mg g^{-1}, 96 mg g^{-1}, 120 mg g^{-1}, and 400 mg g^{-1} at room temperature. Comparing with Zn–Hap, GO, and CA, the fabricated GO@Zn–Hap@CA showed significant increment in adsorption capacity for both Cr(VI) and Pb(II) due to the presence of abundant functional groups. Markedly, although GO had a higher surface area than GO@Zn–Hap@CA, GO behaved differently in aqueous solution.

GO sheets tend to restack, which may have reduced the abundancy of functional groups for adsorbing metal ions in

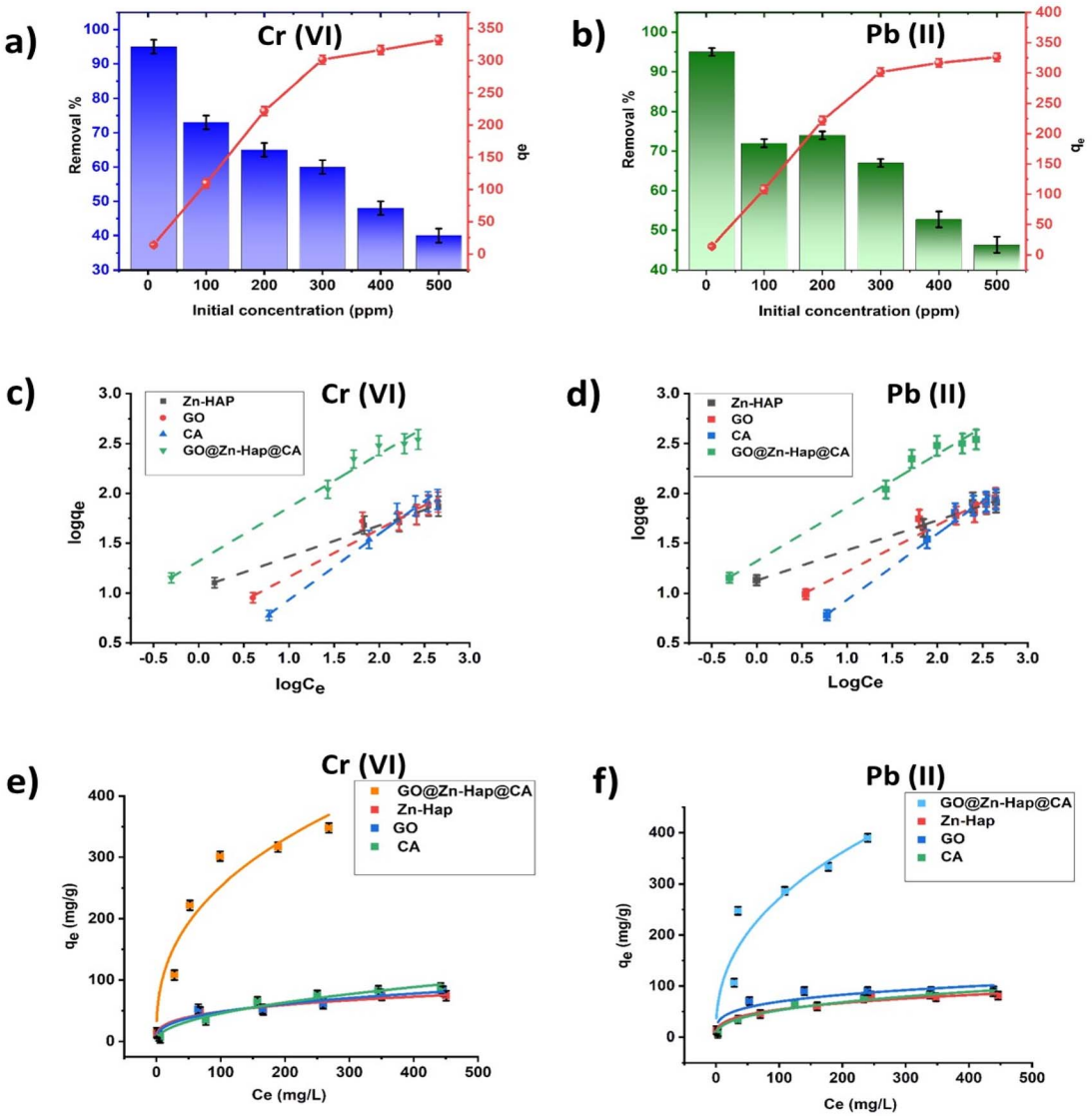

Fig. 7 Effect of the initial Cr(VI) (a) and Pb(II) (b) concentrations on the adsorption capacity and removal efficiency. Linear fitting of the Freundlich isotherm for Cr(IV) (c) and Pb(II) (d). Non-linear fitting of the Freundlich isotherm for Cr(VI) (e) and Pb(II) (f) of Zn–Hap, GO, CA and GO@Zn–Hap@CA; (pH 2 = Cr(VI) and pH 5 = Pb(II),dose 0.05 g; contact time: 100 minutes).

Table 2 Linear isotherm rate constant and regression coefficient value for different models

		Chromium				Lead			
Isotherms	Parameter	Zn–Hap	GO	CA membrane	GO@Zn–Hap@CA	Zn–Hap	GO	CA membrane	GO@Zn–Hap@CA
Langmuir	q_{max} (mg g^{-1})	78	87	113	384	86	96	120	400
	K_L (L mg^{-1})	97	119	140	3908	191	437	84	3358
	R^2	0.9655	0.9513	0.9801	0.9683	0.9766	0.9982	0.9559	0.9572
Frendlich	K_F (mg g^{-1})	11.5	5.4	4.03	21.5	13.3	6.9	2.2	22.8
	n	3.2	2.19	1.55	1.88	3.3	2.1	1.55	2
	R^2	0.9864	0.9489	0.9848	0.9800	0.9889	0.8914	0.9848	0.9975
D–R	Q_m (mg g^{-1})	81	63	60	240	67	68	99	240
	K_{DR} (mol^2 Kj^{-2})	1×10^{-6}	6×10^{-6}	1×10^{-6}	4×10^{-7}	5×10^{-7}	5×10^{-6}	4×10^{-6}	4×10^{-7}
	R^2	0.9237	0.9491	0.9873	0.8829	0.8903	0.9525	0.9942	0.8849
Temkin	A (unitless)	10	14	19	53	15	20	10	73
	K_T (L mg^{-1})	1.7	2.2	5.8	1.4	2.5	2.01	8.48	1.7
	b (kJ mol^{-1})	217	158	117	42	148	108	207	30
	R^2	0.9386	0.937	0.941	0.8742	0.8954	0.9393	0.9957	0.8577

comparison with the composite. The results have revealed that for Cr(VI) and Pb(II), the maximum adsorption capacity of GO@Zn–Hap@CA is 384 mg g^{-1} and 400 mg g^{-1} at room temperature, respectively. This indicates that GO@Zn–Hap@CA has enough adsorption sites, and consequently can reach saturation at a higher Cr(VI) and Pb(II) concentration.

Moreover, in the case of the non-linear isotherm, only the non-linear Freundlich isotherm is well fitted for the composite compared to the other studied isotherms. Fig. 7e and f show the non-linear Freundlich isotherms for Cr(VI) and Pb(II) adsorption on GO, Zn–Hap, CA and GO@Zn–HAP@CA, respectively. The values of the parameters of the non-linear isotherms are provided in Table S1.† Importantly, for both linear and non-linear Freundlich isotherms, the maximum adsorption capacity (K_f) of the GO@Zn–HAP@CA composite is higher than that for Zn–hap, GO and CA, which highlights the increment of adsorption sites in the designed GO@Zn–Hap@CA composite. Thus, the results support the multilayer coverage by the metal ions because of the porosity of the GO@Zn–Hap@CA. Moreover, the n value (1.88 for Cr(VI) and 2 for Pb(II)) in the linear Freundlich isotherm is greater than 1, demonstrating the favorable adsorption phenomenon.

3.5.3 Effects of the contact time and adsorption kinetics study. The effect of the contact time on the Cr(VI) and Pb(II) adsorption is shown in Fig. 8a and b (Cr(VI) concentration: 30–100 mg L^{-1} at pH 2.0, Pb(II) concentration: 30–100 mg L^{-1} at pH 5.0). It was observed that the adsorption capacity increased rapidly within the first 30 minutes. Afterward, it continued to

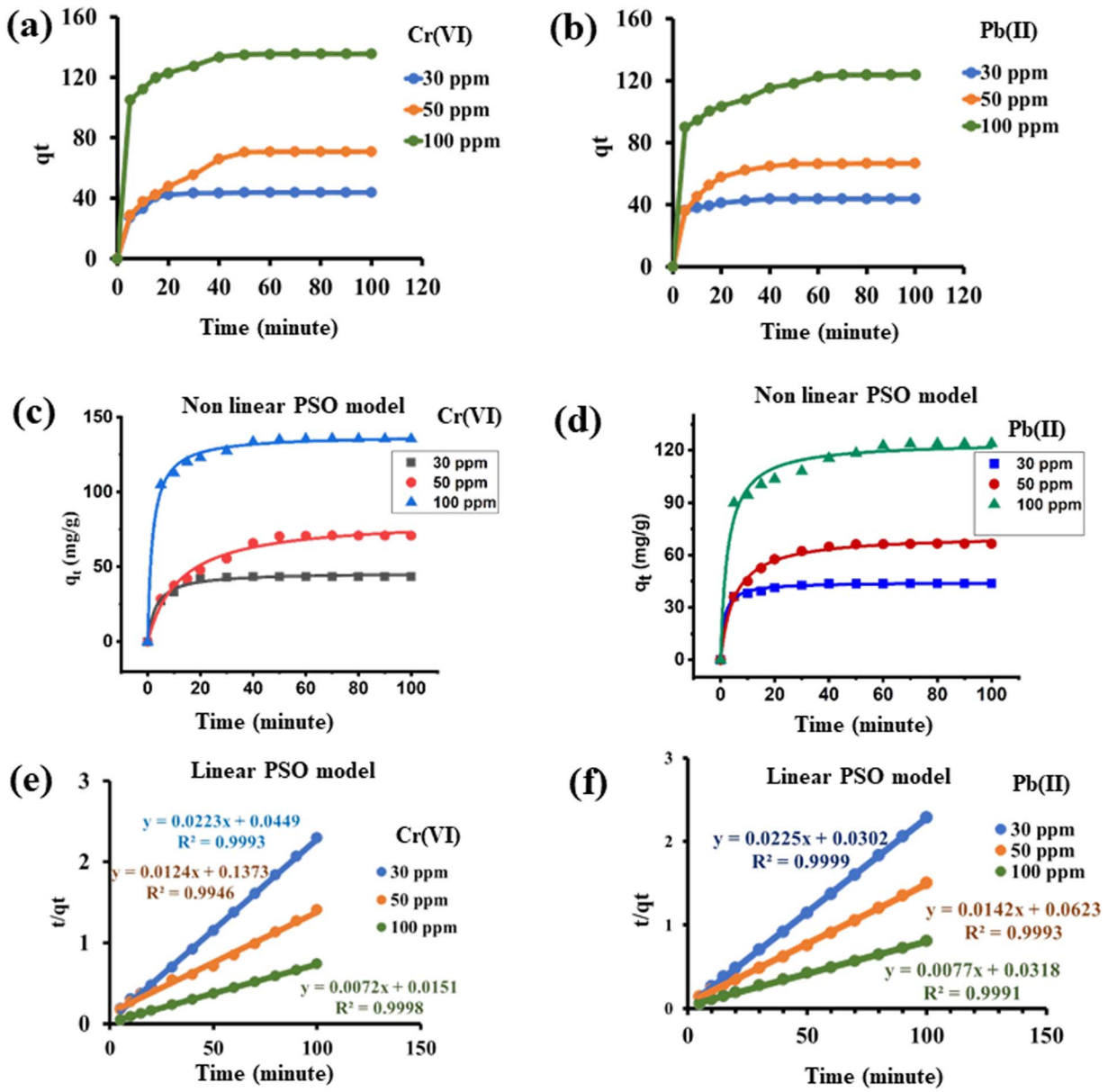

Fig. 8 Effect of contact time on the adsorption of Cr(VI) (a) and Pb(II) (b) onto GO@Zn–HAP@CA. Non-linear fitting of the pseudo second order kinetic model for Cr(VI) (c) and Pb(II) (d). Linear fitting of the pseudo second order kinetic model for Cr(VI) (e) and Pb(II) (f).

Table 3 Comparison of the equilibrium time with other adsorbents of various studies in the literature

Adsorbent	Adsorbate	Equilibrium time	Adsorption condition	Ref.
CA–PCL/CS core–shell nanofibrous adsorbent	Chromium	240 minutes	Metal ion concentration of 200 ppm, adsorbent dosage of 1 g L^{-1}, and pH = 3	69
rGO/PEI-KOH	Chromium	24 hours	Metal ion concentration of100 ppm, adsorbent dosage 1 mg mL^{-1}, pH = 2	70
Fe_3O_4@n-HAp	Chromium	70 minutes	Metal ion concentration of 100 ppm, adsorbent dosage of 0.1 g	71
HAP/Clin/NH_2	Chromium	120 minutes	Metal ion concentration of 50 ppm, adsorbent dosage of 0.05 g, pH = 7	72
GO@Zn–Hap@CA	Chromium	50 minutes	Initial metal concentration = 100 ppm dosage = 0.05 g, pH = 2	This study
20 wt% HAp/Chitosan nanocomposite	Lead	210 minutes	Metal ion concentration of 2000 ppm, adsorbent dosage of 0.1 g, pH = 4	73
Modified CA	Lead	90 minutes	Initial metal concentration = 10 mg L^{-1}, pH ranged from 4.5 to 5.0, dosage = 0.5 g L^{-1}	74
MGO@TNs	Lead	3 hours	Initial concentration = 100 ppm, pH = 5.0	75
Glutathione-functionalized$NiFe_2O_4$/graphene oxide	Lead	90 minutes	Initial concentration = 10 ppm dosage = 10 mg, pH = 5	76
GO@Zn–Hap@CA	Lead	60 minutes	Initial metal concentration = 100 ppm dosage = 0.05 g, pH = 5	This study

increase slowly and reached equilibrium at about 50 minutes for Cr(VI) and 60 minutes for Pb(II). In comparison to other adsorbents reported in various studies in the literature, our designed composite exhibits removal of HMIs in a short period of time. Table 3 represents the equilibrium time of different adsorbents published by other research groups for chromium and lead adsorption. Briefly, most of the adsorbents reached equilibrium after 60 minutes, which exceeds our equilibrium time for the particular adsorption conditions. Hence, our prepared GO@Zn–Hap@CA composite adsorbent is regarded as holding an ultrafast removal capacity in comparison to other adsorbents reported in different studies in the literature.

The kinetics of adsorption of Cr(VI) and Pb(II) onto GO@Zn–Hap@CA were evaluated with both linear and non-linear pseudo-first order, pseudo-second order, and Elovich models by fitting the batch adsorption data. By evaluating the regression coefficient (R^2), it is suggested that the pseudo second order kinetic model of both linear and non-linear isotherms is best suited with the experimental data in comparison to the other kinetic models. The nonlinear and linear fittings of the pseudo second order kinetic model for Cr(VI) and Pb(II) are displayed in Fig. 8c–f. The other studied kinetics models are presented in Fig. S9–S12.† Furthermore, the calculated adsorption capacity (q_m cal) for both Cr(VI) and Pb(II) in the linear and non-linear pseudo-second order kinetic models is closer to that obtained in the experimental data. Thus, the result indicated that the pseudo-second-order model is well-tuned with the experimental data for both Cr(VI) and Pb(II) adsorption. All of the linear kinetics parameters are recorded in Table 4, and the non-linear kinetics parameters are in Table S2.†

3.5.4 Adsorption mechanism. In the composite, there may occur intramolecular and intermolecular H-bonding interactions among the COOH–, OH– of CA, COOH–, OH– functional groups of GO and OH– and $PO4^{2-}$ of Zn–Hap. In this study, FT-IR was applied to better understand the adsorption mechanism of Cr(VI) and Pb(II) on GO@Zn–Hap@CA. The composite exhibits peaks at 3261.8 cm^{-1}, 1587.8 cm^{-1}, 1412.6 cm^{-1}, and 1021.2 cm^{-1}. The discrepancy of the identified functional groups directs the mechanism of adsorption.[4] Fig. 9a shows the FT-IR spectra of GO@Zn–Hap@CA before and after treating with Cr(VI) solutions at pH = 2 and Pb(II) solutions at pH = 5. The functional peaks of GO@Zn–Hap@CA show a range of degrees of red and blue shifts, signifying that the functional sites are involved in the adsorption process. Specifically, when the adsorption process proceeds, the metal ions in the solution chelate with the carboxyl and hydroxyl groups of the GO and CA polymer *via* partly ionic and partly coordinate bonds.[77,78] Additionally, $HCrO4^-$ can attach to the GO@Zn–Hap@CA heterostructure through hydrogen bond.

XPS analysis was used to further elucidate the adsorption mechanism of Cr(VI) and Pb(II) on GO@Zn–Hap@CA. Fig. 9b

Table 4 Different linear kinetic model parameters for Cr(VI) and Pb(II) adsorption

Kinetic model and parameter	Chromium			Lead		
Concentration	30 ppm	50 ppm	100 ppm	30 ppm	50 ppm	100 ppm
Experimental q_e (mg g^{-1})	43.8	72	136.5	43.8	67.5	124.5
Pseudo first order (PFO)						
$q_e$cal (mg g^{-1})	2.06	5.19	4.09	2.05	3.76	5.59
K_1 (min^{-1})	−0.00013	0.000141	−1.27 × 10−4	−0.00016	−0.00012	-1.56×10^{-4}
R^2	0.7053	0.867	0.8705	0.8096	0.8598	0.9565
Pseudo second order (PSO)						
K_2 (g mg^{-1} min^{-1})	0.011076	0.00112	0.003433	0.01676	0.003237	0.00186
q_e cal (mg g^{-1})	44.84	80.6	138.8	44.4	70.4	129.8
R^2	0.9993	0.9946	0.9998	0.9999	0.9993	0.9991
Elovich kinetic model						
α (mg g^{-1} min^{-1})	0.207	0.0623	0.093006	0.37669	0.0981	0.0769
β (g mg^{-1})	4.8544 × 1011	1917.5	9.34255×10^{40}	2.08606×10^{15}	1.54274×10^{12}	1.06042×10^{31}
R^2	0.745	0.9541	0.9473	0.907	0.913	0.9742

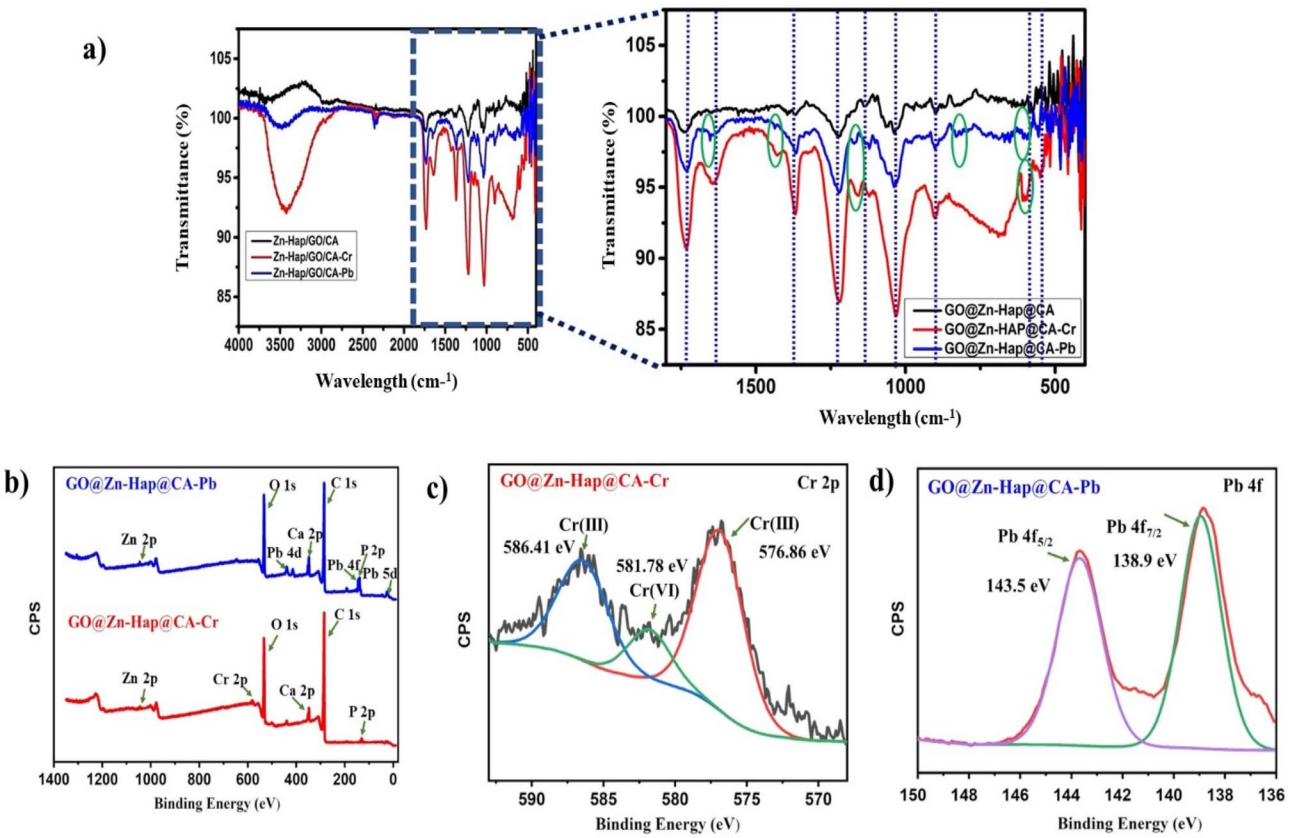

Fig. 9 (a) FTIR analysis after adsorption of Cr(VI) and Pb(II) on GO@Zn–Hap@CA; XPS survey spectrum of Cr(VI) and Pb(II) adsorbed GO@Zn–Hap@CA (b); XPS deconvoluted Cr 2p spectra (c) and Pb 4f spectra (d).

demonstrates the survey spectrum of the Cr(VI) and Pb(II) loaded GO@Zn–Hap@CA composite. After Cr(VI) adsorption, in contrast with the XPS spectrum of GO@Zn–Hap@CA (Fig. 2), a new peak of binding energy (B.E) 577 eV arises in the GO@Zn–Hap@CA-Cr(VI) spectrum (Fig. 9b), which verifies the presence of chromium. The Cr 2p spectrum (Fig. 9c) is deconvoluted into peaks at 576.86 eV and 586.41 eV, which resembles the Cr $2p_{3/2}$ and Cr $2p_{1/2}$ states of Cr(III), while the peaks at 581.78 eV correspond to the Cr $2p_{3/2}$ state of Cr(VI).[79] In the composite, there exists abundant amounts of carboxyl groups from GO and CA, and hydroxyl groups from Zn–Hap, GO and CA. The excessive amount of –C=O, –OH groups can be readily protonated in the acidic environment that contributes to the reduction of Cr(VI) to Cr(III), which is less toxic than Cr(VI).[70] The

following mentioned redox reactions are suggested to have involvement in the reduction of Cr(VI) to Cr(III).[80]

$$\text{R-CH}_2\text{-OH} + \text{Cr(VI)} \rightarrow \text{R-(C=O) H} + \text{Cr(III)} \quad (22)$$

$$\text{R-(C=O) H} + \text{Cr(VI)} \rightarrow \text{R-COOH} + \text{Cr(III)} \quad (23)$$

Moreover, in the presence of a π-electron donor, the six-member aromatic ring of GO, more Cr(VI) was profoundly reduced to Cr(III) in the acidic media. Therefore, the intensity of signal for Cr(VI) was found to be lower than Cr(III). The successive reduction of Cr(VI) to Cr(III) occurred by the following reactions:[79]

$$HCrO_4^- + 7H^+ + 3e^- \rightarrow Cr^{3+} + 4H_2O \quad (24)$$

$$Cr_2O_7^{2-} + 14H^+ + 6e^- \rightarrow 2Cr^{3+} + 7H_2O \quad (25)$$

In similar context, after Pb(II) adsorption (Fig. 9b), the characteristic peaks are detected for Pb 4d, Pb 4f, Pb 5d, at binding energies of 434 eV, 140 eV and 18 eV, respectively which confirms the adsorption of Pb(II) onto the GO@Zn–Hap@CA surface. Moreover, the high-resolution deconvoluted spectra at 138.9 eV and 143.5 eV in Fig. 9d are linked to the Pb $4f_{7/2}$ and Pb $4f_{5/2}$ states of Pb(II) adsorbed on the composite surface.[81,82] Noticeably, after adsorption of HMIs, all other deconvoluted spectra of C1s, O 1s, Ca 2p, P 2p, and Zn 2s (Fig. S13 and S14†) of the HMIs loaded-composite show a slight shifting in the binding energy compared to the composite before adsorption. Hence, the involvement of these groups in the adsorption phenomenon is verified.

Moreover, FESEM-EDX analysis of chromium (Fig. S15a†) and lead (Fig. S15b†) adsorbed on GO@Zn–Hap@CA discloses the presence of chromium and lead elements in the heterostructure. Fig. 10 illustrates the mechanism of adsorption of metal ions on GO@Zn–Hap@CA. Briefly, it is suggested that three types of features (including electrostatic, H-bond, and chelate formation) between the metal ions and adsorbate govern the removal of Cr(VI) and Pb(II) from aqueous media.

3.5.5 Effects of Co-existing ions. Real wastewater typically contains a variety of cations and anions that affect the adsorption performance of the target metal ions. The influence of co-existing negative ions (anions: SO_4^{2-}, Cl^-, NO_3^-, $HCrO_4^-$) and positive ions (cations: Cd^{2+}, Cu^{2+}, Mn^{2+}, Pb^{2+}) has been examined for their effects on Cr(VI) and Pb(II) adsorption by GO@Zn–Hap@CA. The concentrations of Cr(VI) and Pb(II) solutions were kept at 100 mg L^{-1}. Here, other co-existing ions were mixed with varying concentrations of both anions and cations from a concentration range of 10–30 mg L^{-1} at pH = 2.0 for Cr(VI) and pH = 5 for Pb(II).

From the experiment, it is evidently observed in Fig. 11a that cations (Cd^{2+}, Cu^{2+}, Mn^{2+}, Pb^{2+}) did not interfere with Cr(VI) adsorption on GO@Zn–Hap@CA at pH = 2. This is because of the fact that at lower pH, the adsorption surface is positively charged. This implies that there was repulsion between the

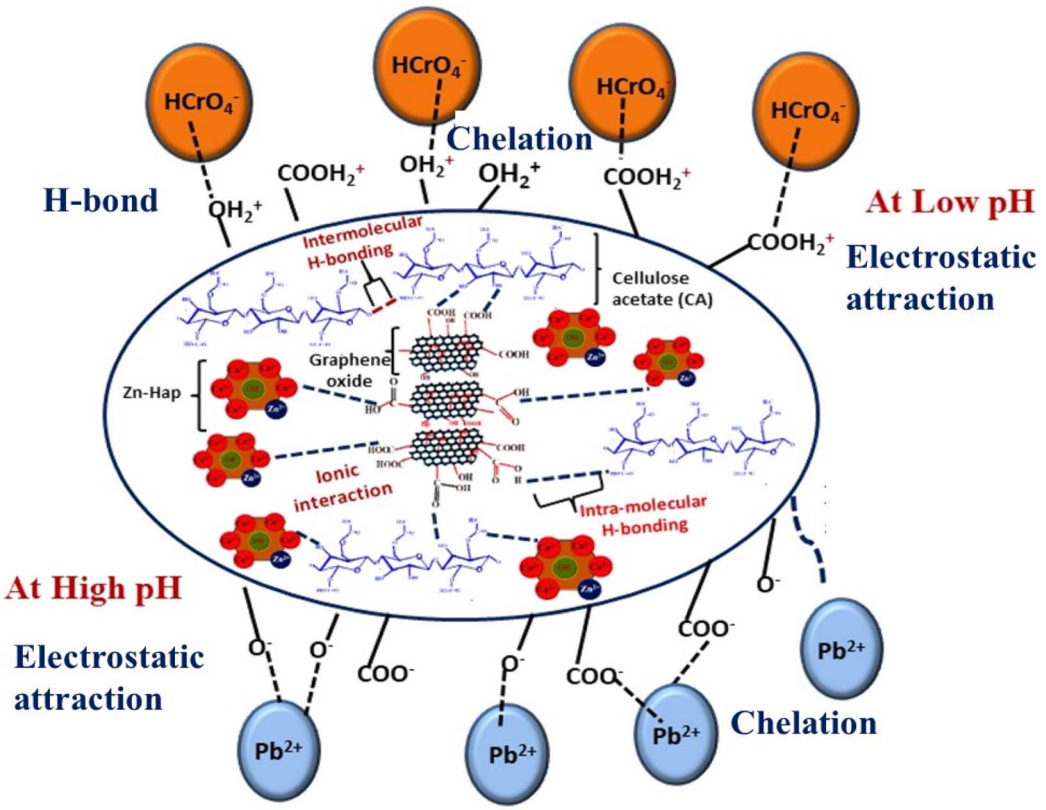

Fig. 10 Schematic representation of the mechanism of interaction with Cr(VI) and Pb(II).

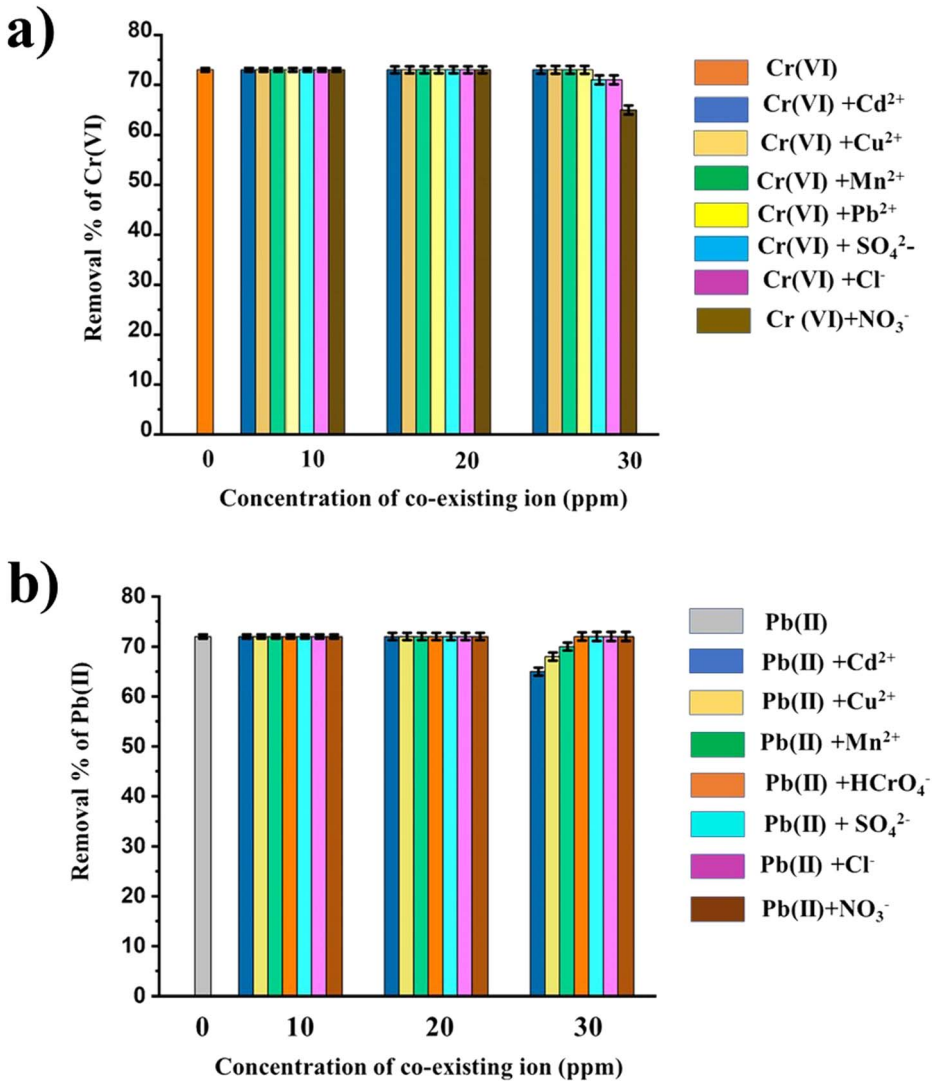

Fig. 11 (a) Effect of co-existing ions on Cr(VI) removal by GO@Zn–Hap@CA. (b) Effect of co-existing ions on Pb(II) removal by GO@Zn–Hap@CA.

positively charged cations on the adsorbent surface, thus facilitating the adsorption of the negatively charged chromate. Moreover, SO_4^{2-}, Cl^-, and NO_3^- are low affinity ligands,[83] which implies less adsorption, and thus less competition with Cr(VI) ions at their lower concentration. Hence, adsorption of Cr(VI) by GO@Zn–Hap@CA is slightly decreased (from 73% to 71% for Cl^-, from 73% to 71% for NO_3^-, and from 73% to 65% for SO_4^{2-}) at 30 ppm co-existing ions. Thus, the results signify the promising potency of the adsorbent.

In the case of Pb(II) (Fig. 11b), the percentage removal of Pb(II) was not changed when the concentration of the co-existing cations (Cd^{2+}, Cu^{2+}, Mn^{2+}) was increased up to 20 ppm. However, the concentration was decreased slightly (from 72% to 65% for Cu^{2+}, 72% to 68% for Cd^{2+}, 72% 70% for Mn^{2+}) when it increased to 30 ppm. This may be because of the competition for the active sites on the adsorbent. Mainly, the characteristic covalent index ($X^2_m r$, where X_m defines the electronegativity and r denotes the ionic radius) governs the selective adsorption of Pb(II) by GO@Zn–Hap@CA. The larger the value of $X^2_m r$, the more the metal ions favorably interact with the active functional sites.[84] Notably, the covalent index is decreased in the following order: Pb (6.41) > Cu (2.98) > Cd (2.71) > Mn(II) (1.97),[85] indicating that Pb(II) has an intense attraction to the functional sites of the adsorbent when compared to Cu, Cd, and Mn. In the case of the coexisting anionic species ($SO4^2$, Cl^-, $NO3^-$ $HCrO_4^-$) at pH = 5, the adsorbent surface is negatively charged, which generates repulsion between the negatively charged surface and anions. This situation promotes the easy adsorption of positive Pb(II) metal ions. These results recommended that Pb(II) could be successfully removed using GO@Zn–Hap@CA, despite the existence of inferring ions.

3.5.6 Regeneration and reuse of GO@Zn–Hap@CA. The recyclability of adsorbents is an important aspect, particularly with regard to energy consumption, economic efficiency and environmental sustainability. Hence, an experiment was carried out on multi-cycle to evaluate the potency of GO@Zn–Hap@CA with regard to the repetitive adsorption of Cr(VI) and Pb(II).

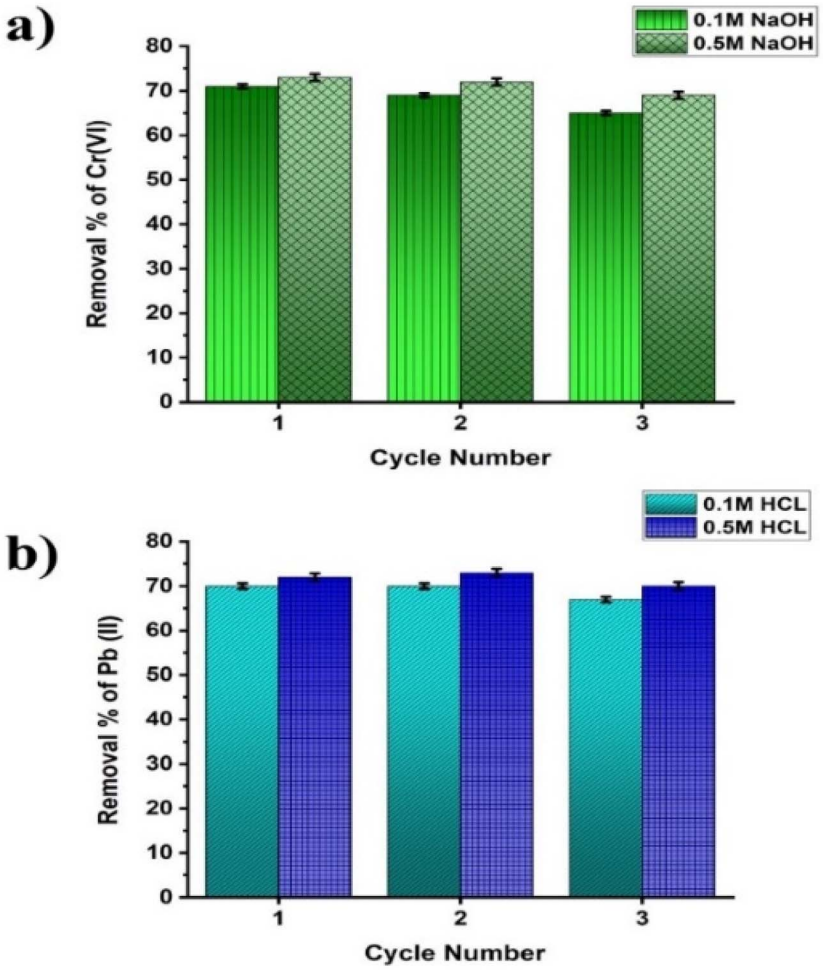

Fig. 12 (a) Removal efficiency of Cr(VI) ions of each cycle after desorption with NaOH. (b) Removal efficiency of Pb(II) ions of each cycle after desorption with HCl.

GO@Zn–Hap@CA was regenerated using 30 mL of different concentrations of (0.1 M and 0.5 M) NaOH and (0.1 M and 0.5 M) HCl for Cr(VI) and Pb(II), respectively. Here, a low concentration of solvent was used, as an extremely higher concentration may destroy the structure of the exhausted adsorbent. To inspect the competence of the regenerated adsorbents, GO@Zn–Hap@CA was washed with deionized water and air dried. Next, the regenerated adsorbents were used for the adsorption of Cr(VI) and Pb(II) at 100 mg L^{-1} for 100 minutes.

Fig. 12 illustrates that the removal% of HMIs is more when a high concentration solvent is used for desorption. It is plausible that the amount of hydrogen ions and hydroxyl ions is responsible for the desorption effectiveness *via* ion exchange process with positively charged and negatively charged metal ions. Herein, the Cr(VI) removal (%) was decreased from 73% to 69% from the first cycle to the third cycle when 0.5 M NaOH was used. Pb(II) removal (%) was decreased from 72% to 70% from the first cycle to the third cycle when 0.5 M HCl was used. This decrease in adsorption efficiency is possibly because of the partial desorption, as well as irreversible chelate formation, of Cr(VI) and Pb(II) onto the GO@Zn–Hap@CA surface. Therefore, it is evident that the GO@Zn–Hap@CA could be reused for the removal of Cr(VI) and Pb(II) from polluted water for up to three consecutive cycles. Table 5 shows the comparison of different

Table 5 The maximum adsorption capacity of Cr(VI) and Pb(II) compared with other reported work

Adsorbate	Adsorbent	Q_{max}	Ref.
Chromium	RGO/Hat hybrid composite	45.2	86
	Chitosan grafted GO nanocomposite	292.8	87
	Chitosan/GO	310.4	88
	Sr-Hap	443	89
	RGO-PEI-KOH	398.9	31
	GO@Zn–Hap@CA	384	This study
Lead	GO from waste dry cell battery	55.8	90
	GO/alginate hydrogel	118.6	4
	Nanohydroxyapatite	192.3	91
	Mg–Hap	218	34
	EDTA functionalized magnetic GO	268.4	92
	GO@Zn–Hap@CA	400	This study

GO, doped hap-based adsorbents for chromium and lead removal with the new developed adsorbent. It is clearly evident from Table 5 that the GO@Zn–Hap@CA exhibits high adsorption capacity (q_{max}), and therefore endows extreme potentials for the removal of the Cr(VI) and Pb(II) ions from aqueous media.

4 Conclusions

In summary, GO@Zn–Hap@CA was successfully fabricated in the form of a well-built structure. The crosslinking interaction *via* intramolecular and intermolecular H-bonds within the molecules of the GO@Zn–Hap@CA heterostructure was confirmed by FT-IR and XPS. A remarkable average roughness (R_a) of about 137 nm and root mean square roughness (R_q) of about 194 nm are credited for the favorable decrease of Cr(VI) and Pb(II) ions from aqueous solution. Notably, the high surface area and mesoporous texture of about 4.52 nm also enhanced the removal of Cr(VI) and Pb(II) ions. Batch adsorption experiments confirmed that GO@Zn–Hap@CA possesses a high linear Langmuir adsorption capacity, 384 mg g^{-1} for Cr(VI) at pH = 2 and 400 mg g^{-1} for Pb(II) at pH = 5. Moreover, rapid removal of Cr(VI) and Pb(II) was observed within 50 minutes and 60 minutes, respectively. The adsorption process was fitted well to the linear and non-linear pseudo-second-order models and linear Freundlich model. Significantly, the mechanism of adsorption by XPS indicates the adsorption of lead and chromium to the functional sites, and affirms the reduction of toxic chromium(VI) to the less toxic Cr(III). Effects of the co-existing ions reveal that up to 20 ppm concentration of co-existing ions had no impact on the adsorption potency. In addition, after three adsorption–desorption cycles, the GO@Zn–Hap@CA exhibits 69% and 70% removal efficiency of Cr(VI) and Pb(II), respectively, signifying its excellent recyclability. This work offers a new heterostructured adsorbent to eliminate the potentially hazardous heavy metals from wastewater.

Author contributions

Monika Mahmud designed the research plan, conducted the experiments, and wrote the manuscript. Md. Sahadat Hossain conducted the batch experiments. Mashrafi Bin Mobarak conducted the batch experiments. Md. Saiful Quddus conducted the experiment for surface area and porosity analysis. Muhammad Shahriar Bashar conducted the experiment for roughness analysis. Umme Sarmeen Akhtar conducted the experiment for XPS analysis. Shirin Akter Jahan contributed to all of the experiments and analysis. Dipa Islam conducted the experiment for the morphological investigation. Samina Ahmed supervised the entire research work and contributed to the entire experimental analysis.

Conflicts of interest

There is no conflict of interest to report.

Acknowledgements

We gratefully acknowledge the Bangladesh Council of Scientific and Industrial Research (BCSIR) authority for approving the R&D project (R&D ref. No. 39.02.0000.011.14.128.2020.636, Date 29.12.2020).

References

1 R. Al-Wafi, M. K. Ahmed and S. F. Mansour, Tuning the synthetic conditions of graphene oxide/magnetite/hydroxyapatite/cellulose acetate nanofibrous membranes for removing Cr (VI), Se (IV) and methylene blue from aqueous solutions, *J. Water Process Eng.*, 2020, **38**, 101543.
2 M. Feng, P. Zhang, H. C. Zhou and V. K. Sharma, Water-stable metal-organic frameworks for aqueous removal of heavy metals and radionuclides: A review, *Chemosphere*, 2018, **209**, 783–800.
3 P. C. Bandara, J. Peña-Bahamonde and D. F. Rodrigues, Redox mechanisms of conversion of Cr (VI) to Cr (III) by graphene oxide-polymer composite, *Sci. Rep.*, 2020, **10**(1), 1–8.
4 C. Bai, L. Wang and Z. Zhu, Adsorption of Cr (III) and Pb (II) by graphene oxide/alginate hydrogel membrane: Characterization, adsorption kinetics, isotherm and thermodynamics studies, *Int. J. Biol. Macromol.*, 2020, **147**, 898–910.
5 S. M. Anush and B. Vishalakshi, Modified chitosan gel incorporated with magnetic nanoparticle for removal of Cu (II) and Cr (VI) from aqueous solution, *Int. J. Biol. Macromol.*, 2019, **133**, 1051–1062.
6 A. Vengosh, R. Coyte, J. Karr, J. S. Harkness, A. J. Kondash, L. S. Ruhl, *et al.*, Origin of hexavalent chromium in drinking water wells from the piedmont aquifers of North Carolina, *Environ. Sci. Technol. Lett.*, 2016, **3**(12), 409–414.
7 M. Mahmud, M. Sahadat Hossain, M. Bin Mobarak, S. Sultana, S. Sharmin and S. Ahmed, Co-precipitation synthesis of non-cytotoxic and magnetic cobalt ferrite nanoparticles for purging heavy metal from the aqueous medium: Pb (II) adsorption isotherms and kinetics study, *Chem. Ecol.*, 2022, **38**(6), 544–563.
8 K. A. Kumar, B. Lakshminarayana, D. Suryakala and C. Subrahmanyam, Reduced graphene oxide supported ZnO quantum dots for visible light-induced simultaneous removal of tetracycline and hexavalent chromium, *RSC Adv.*, 2020, **10**(35), 20494–20503.
9 S. Habibi, A. Nematollahzadeh and S. A. Mousavi, Nano-scale modification of polysulfone membrane matrix and the surface for the separation of chromium ions from water, *Chem. Eng. J.*, 2015, **267**, 306–316.
10 Z. Wu, W. Huang, X. Shan and Z. Li, Preparation of a porous graphene oxide/alkali lignin aerogel composite and its adsorption properties for methylene blue, *Int. J. Biol. Macromol.*, 2020, **143**, 325–333.
11 W. Wei, X. Han, M. Zhang, Y. Zhang and C. Zheng, Macromolecular humic acid modified nano-hydroxyapatite for simultaneous removal of Cu (II) and methylene blue from aqueous solution: experimental design and adsorption study, *Int. J. Biol. Macromol.*, 2020, **150**, 849–860.
12 M. S. Moorthy, D. J. Seo, H. J. Song, S. S. Park and C. S. Ha, Magnetic mesoporous silica hybrid nanoparticles for highly

selective boron adsorption, *J. Mater. Chem. A*, 2013, **1**(40), 12485–12496.
13 F. Fu and Q. Wang, Removal of heavy metal ions from wastewaters: a review, *J. Environ. Manage.*, 2011, **92**(3), 407–418.
14 N. K. Mondal and S. Chakraborty, Adsorption of Cr (VI) from aqueous solution on graphene oxide (GO) prepared from graphite: equilibrium, kinetic and thermodynamic studies, *Appl. Water Sci.*, 2020, **10**(2), 1–10.
15 P. Yuan, M. Fan, D. Yang, H. He, D. Liu, A. Yuan, *et al.*, Montmorillonite-supported magnetite nanoparticles for the removal of hexavalent chromium [Cr (VI)] from aqueous solutions, *J. Hazard. Mater.*, 2009, **166**(2–3), 821–829.
16 P. K. Mishra, R. Kumar and P. K. Rai, Surfactant-free one-pot synthesis of CeO 2, TiO 2 and Ti@ Ce oxide nanoparticles for the ultrafast removal of Cr (vi) from aqueous media, *Nanoscale*, 2018, **10**(15), 7257–7269.
17 F. Latifeh, Y. Yamini and S. Seidi, Ionic liquid-modified silica-coated magnetic nanoparticles: promising adsorbents for ultra-fast extraction of paraquat from aqueous solution, *Environ. Sci. Pollut. Res. Int.*, 2016, **23**(5), 4411–4421.
18 B. Zheng, X. Lin, X. Zhang, D. Wu and K. Matyjaszewski, Emerging functional porous polymeric and carbonaceous materials for environmental treatment and energy storage, *Adv. Funct. Mater.*, 2020, **30**(41), 1907006.
19 J. Mei, H. Zhang, S. Mo, Y. Zhang, Z. Li and H. Ou, Prominent adsorption of Cr (VI) with graphene oxide aerogel twined with creeper-like polymer based on chitosan oligosaccharide, *Carbohydr. Polym.*, 2020, **247**, 116733.
20 K. S. Novoselov, A. K. Geim, S. V. Morozov, D. Jiang eng, Y. Zhang, S. V. Dubonos, *et al.*, Electric field effect in atomically thin carbon films, *Science*, 2004, **306**(5696), 666–669.
21 H. Wu, L. Li, K. Chang, K. Du, C. Shen, S. Zhou, *et al.*, Graphene oxide decorated nanoscale iron sulfide for highly efficient scavenging of hexavalent chromium from aqueous solutions, *J. Environ. Chem. Eng.*, 2020, **8**(4), 103882.
22 S. M. Anush, H. R. Chandan, B. H. Gayathri, N. Manju, B. Vishalakshi and B. Kalluraya, Graphene oxide functionalized chitosan-magnetite nanocomposite for removal of Cu (II) and Cr (VI) from waste water, *Int. J. Biol. Macromol.*, 2020, **164**, 4391–4402.
23 Y. Yoon, M. Zheng, Y. T. Ahn, W. K. Park, W. S. Yang and J. W. Kang, Synthesis of magnetite/non-oxidative graphene composites and their application for arsenic removal, *Sep. Purif. Technol.*, 2017, **178**, 40–48.
24 L. Yang, F. Jia and S. Song, Recovery of [Au (CN) 2]- from gold cyanidation with graphene oxide as adsorbent, *Sep. Purif. Technol.*, 2017, **186**, 63–69.
25 S. Bao, W. Yang, Y. Wang, Y. Yu, Y. Sun and K. Li, PEI grafted amino-functionalized graphene oxide nanosheets for ultrafast and high selectivity removal of Cr (VI) from aqueous solutions by adsorption combined with reduction: Behaviors and mechanisms, *Chem. Eng. J.*, 2020, **399**, 125762.
26 M. Shaban, M. R. Abukhadra, M. Rabia, Y. A. Elkader and M. R. Abd El-Halim, Investigation the adsorption properties of graphene oxide and polyaniline nano/micro structures for efficient removal of toxic Cr(VI) contaminants from aqueous solutions; kinetic and equilibrium studies, *Atti Accad. Naz. Lincei, Cl. Sci. Fis., Mat. Nat., Rend.*, 2018, **29**(1), 141–154.
27 J. Geng, Y. Yin, Q. Liang, Z. Zhu and H. Luo, Polyethyleneimine cross-linked graphene oxide for removing hazardous hexavalent chromium: Adsorption performance and mechanism, *Chem. Eng. J.*, 2019, **361**, 1497–1510.
28 M. Yan, W. Huang and Z. Li, Chitosan cross-linked graphene oxide/lignosulfonate composite aerogel for enhanced adsorption of methylene blue in water, *Int. J. Biol. Macromol.*, 2019, **136**, 927–935.
29 L. Liu, C. Li, C. Bao, Q. Jia, P. Xiao, X. Liu, *et al.*, Preparation and characterization of chitosan/graphene oxide composites for the adsorption of Au (III) and Pd (II), *Talanta*, 2012, **93**, 350–357.
30 A. A. Yakout, R. H. El-Sokkary, M. A. Shreadah and O. G. A. Hamid, Cross-linked graphene oxide sheets *via* modified extracted cellulose with high metal adsorption, *Carbohydr. Polym.*, 2017, **172**, 20–27.
31 Y. Tadjenant, N. Dokhan, A. Barras, A. Addad, R. Jijie, S. Szunerits, *et al.*, Graphene oxide chemically reduced and functionalized with KOH-PEI for efficient Cr (VI) adsorption and reduction in acidic medium, *Chemosphere*, 2020, **258**, 127316.
32 S. Pai, S. M. Kini, R. Selvaraj and A. Pugazhendhi, A review on the synthesis of hydroxyapatite, its composites and adsorptive removal of pollutants from wastewater, *J. Water Process Eng.*, 2020, **38**, 101574.
33 J. K. Rajak, N. Khandelwal, M. P. Behera, E. Tiwari, N. Singh, Z. A. Ganie, *et al.*, Removal of chromate ions from leachate-contaminated groundwater samples of Khan Chandpur, India, using chitin modified iron-enriched hydroxyapatite nanocomposite, *Environ. Sci. Pollut. Res.*, 2021, **28**(31), 41760–41771.
34 M. Zhou, X. Yan, H. Zou, Y. Zhao, N. Yin, C. Zhang, *et al.*, Enhanced adsorption of Pb (II) from aqueous solution by magnesium-incorporated hydroxyapatite with poor crystalline structure, *Desalin. Water Treat.*, 2019, **171**, 183–195.
35 S. Campisi, C. Evangelisti, G. Postole and A. Gervasini, Combination of interfacial reduction of hexavalent chromium and trivalent chromium immobilization on tin-functionalized hydroxyapatite materials, *Appl. Surf. Sci.*, 2021, **539**, 148227.
36 A. Fakharzadeh, R. Ebrahimi-Kahrizsangi, B. Nasiri-Tabrizi and W. J. Basirun, Effect of dopant loading on the structural features of silver-doped hydroxyapatite obtained by mechanochemical method, *Ceram. Int.*, 2017, **43**(15), 12588–12598.

37 V. K. Gupta, P. J. M. Carrott, R. Singh, M. Chaudhary and S. Kushwaha, Cellulose: a review as natural, modified and activated carbon adsorbent, *Bioresour. Technol.*, 2016, **216**, 1066–1076.

38 A. ZabihiSahebi, S. Koushkbaghi, M. Pishnamazi, A. Askari, R. Khosravi and M. Irani, Synthesis of cellulose acetate/chitosan/SWCNT/Fe3O4/TiO2 composite nanofibers for the removal of Cr(VI), As(V), Methylene blue and Congo red from aqueous solutions, *Int. J. Biol. Macromol.*, 2019, **140**, 1296–1304.

39 S. F. Mansour, R. Al-Wafi, M. K. Ahmed and S. Wageh, Microstructural, morphological behavior and removal of Cr (VI) and Se (IV) from aqueous solutions by magnetite nanoparticles/PVA and cellulose acetate nanofibers, *Appl. Phys. A*, 2020, **126**(3), 1–14.

40 N. I. Zaaba, K. L. Foo, U. Hashim, S. J. Tan, W. W. Liu and C. H. Voon, Synthesis of Graphene Oxide using Modified Hummers Method: Solvent Influence, *Procedia Eng.*, 2017, **184**, 469–477.

41 H. Yu, B. Zhang, C. Bulin, R. Li and R. Xing, High-efficient synthesis of graphene oxide based on improved hummers method, *Sci. Rep.*, 2016, **6**(1), 1–7.

42 C. A. Guerrero-Fajardo, L. Giraldo and J. C. Moreno-Piraján, Graphene Oxide: Study of Pore Size Distribution and Surface Chemistry Using Immersion Calorimetry, *Nanomaterials*, 2020, **10**(8), 1492.

43 V. B. Mohan, K. Jayaraman and D. Bhattacharyya, Brunauer–Emmett–Teller (BET) specific surface area analysis of different graphene materials: a comparison to their structural regularity and electrical properties, *Solid State Commun.*, 2020, **320**, 114004.

44 B. Gurzęda, T. Buchwald, M. Nocuń, A. Bąkowicz and P. Krawczyk, Graphene material preparation through thermal treatment of graphite oxide electrochemically synthesized in aqueous sulfuric acid, *RSC Adv.*, 2017, **7**(32), 19904–19911.

45 A. M. Pandele, A. Constantinescu, I. C. Radu, F. Miculescu, S. Ioan Voicu and L. T. Ciocan, Synthesis and characterization of pla-micro-structured hydroxyapatite composite films, *Materials*, 2020, **13**(2), 274.

46 I. Langmuir, The adsorption of gases on plane surfaces of glass, mica and platinum, *J. Am. Chem. Soc.*, 1918, **40**(9), 1361–1403.

47 H. Freundlich, Über die adsorption in lösungen, *Z. Phys. Chem.*, 1907, **57**(1), 385–470.

48 Y. S. Ho, J. F. Porter and G. McKay, Equilibrium isotherm studies for the sorption of divalent metal ions onto peat: copper, nickel and lead single component systems, *Water Air Soil Pollut.*, 2002, **141**(1), 1–33.

49 M. I. Temkin, Kinetics of ammonia synthesis on promoted iron catalysts, *Acta physiochim URSS*, 1940, **12**, 327–356.

50 S. K. Lagergren, About the theory of so-called adsorption of soluble substances, *Sven Vetenskapsakad Handingarl*, 1898, **24**, 1–39.

51 Y. S. Ho and G. McKay, Sorption of dye from aqueous solution by peat, *Chem. Eng. J.*, 1998, **70**(2), 115–124.

52 C. Aharoni and F. C. Tompkins, Kinetics of Adsorption and Desorption and the Elovich Equation, in *Advances in Catalysis [Internet]*, ed. D. D. Eley, H. Pines and P. B. Weisz, Academic Press, 1970 pp. 1–49. Available from: **https://www.sciencedirect.com/science/article/pii/S0360056408605635**.

53 C. L. Popa, A. Deniaud, I. Michaud-Soret, R. Guégan, M. Motelica-Heino and D. Predoi, Structural and Biological Assessment of Zinc Doped Hydroxyapatite Nanoparticles, *J. Nanomater.*, 2016, **2016**, e1062878.

54 S. F. Kabir, S. Ahmed, M. Ahsan and A. I. Mustafa, Investigation of sintering temperature and concentration effects on Zn substituted HA, *Trends Biomater. Artif. Organs*, 2011, **25**(4), 154–160.

55 M. K. Ahmed, M. Afifi, N. S. Awwad and H. A. Ibrahium, Pb (II) and Cd (II) removal, mechanical and morphological features of nanofibrous membranes of cellulose acetate containing fillers of hydroxyapatite, graphene oxide, and magnetite, *Appl. Phys. A*, 2020, **126**(10), 1–12.

56 Y. Mu, K. Zhu, J. Luan, S. Zhang, C. Zhang, R. Na, *et al.*, Fabrication of hybrid ultrafiltration membranes with improved water separation properties by incorporating environmentally friendly taurine modified hydroxyapatite nanotubes, *J. Membr. Sci.*, 2019, **577**, 274–284.

57 M. Abolhassani, C. S. Griggs, L. A. Gurtowski, J. A. Mattei-Sosa, M. Nevins, V. F. Medina, *et al.*, Scalable chitosan-graphene oxide membranes: The effect of GO size on properties and cross-flow filtration performance, *ACS Omega*, 2017, **2**(12), 8751–8759.

58 H. Song ming, L. Zhu jing, Z. Zeng xiang and Q. Xue ji, High performance forward osmosis cellulose acetate (CA) membrane modified by polyvinyl alcohol and polydopamine, *J. Polym. Res.*, 2018, **25**(7), 1–8.

59 H. Zhang, Y. Liang, X. Wu and H. Zheng, Enhanced photocatalytic activity of (Zn, N)-codoped TiO2 nanoparticles, *Mater. Res. Bull.*, 2012, **47**(9), 2188–2192.

60 A. A. Menazea and M. K. Ahmed, Silver and copper oxide nanoparticles-decorated graphene oxide *via* pulsed laser ablation technique: Preparation, characterization, and photoactivated antibacterial activity, *Nano-Struct. Nano-Objects*, 2020, **22**, 100464.

61 R. K. S. Rathour, J. Bhattacharya and A. Mukherjee, Selective and multicycle removal of Cr (VI) by graphene oxide–EDTA composite: insight into the removal mechanism and ionic interference in binary and ternary associations, *Environ. Technol. Innovation*, 2020, **19**, 100851.

62 S. Luanwuthi, A. Krittayavathananon, P. Srimuk and M. Sawangphruk, In situ synthesis of permselective zeolitic imidazolate framework-8/graphene oxide composites: rotating disk electrode and Langmuir adsorption isotherm, *RSC Adv.*, 2015, **5**(58), 46617–46623.

63 L. Fan, C. Luo, M. Sun and H. Qiu, Synthesis of graphene oxide decorated with magnetic cyclodextrin for fast

chromium removal, *J. Mater. Chem.*, 2012, **22**(47), 24577–24583.

64 S. I. Shupack, The chemistry of chromium and some resulting analytical problems, *Environ. Health Perspect.*, 1991, **92**, 7–11.

65 K. C. Lai, L. Y. Lee, B. Y. Z. Hiew, S. Thangalazhy-Gopakumar and S. Gan, Facile synthesis of xanthan biopolymer integrated 3D hierarchical graphene oxide/titanium dioxide composite for adsorptive lead removal in wastewater, *Bioresour. Technol.*, 2020, **309**, 123296.

66 J. H. Roque-Ruiz, J. A. Garibay-Alvarado, N. A. Medellín-Castillo and S. Y. Reyes-López, Preparation of Electrospun Hydroxyapatite-Glass Fibers for Removal of Cadmium (Cd+ 2) and Lead (Pb+ 2) from Aqueous Media, *Water Air Soil Pollut.*, 2020, **231**(10), 1–13.

67 R. Gong, K. Zhong, Y. Hu, J. Chen and G. Zhu, Thermochemical esterifying citric acid onto lignocellulose for enhancing methylene blue sorption capacity of rice straw, *J. Environ. Manage.*, 2008, **88**(4), 875–880.

68 M. Kılıc, C. Kırbıyık, Ö. Çepelioğullar and A. E. Pütün, Adsorption of heavy metal ions from aqueous solutions by bio-char, a by-product of pyrolysis, *Appl. Surf. Sci.*, 2013, **283**, 856–862.

69 L. Ma, X. Shi, X. Zhang, S. Dong and L. Li, Electrospun cellulose acetate–polycaprolactone/chitosan core–shell nanofibers for the removal of Cr (VI), *Phys. Status Solidi A*, 2019, **216**(22), 1900379.

70 Y. Tadjenant, N. Dokhan, A. Barras, A. Addad, R. Jijie, S. Szunerits, *et al.*, Graphene oxide chemically reduced and functionalized with KOH-PEI for efficient Cr (VI) adsorption and reduction in acidic medium, *Chemosphere*, 2020, **258**, 127316.

71 V. Gopalakannan, S. Periyasamy and N. Viswanathan, Fabrication of magnetic particles reinforced nano-hydroxyapatite/gelatin composite for selective Cr (VI) removal from water, *Environ. Sci.: Water Res. Technol.*, 2018, **4**(6), 783–794.

72 M. Zendehdel, K. Rezaeian, A. Rezaei and S. Jalalvandi, Synthesis and Characterization of a Low-Cost and Eco-friendly Hydroxyapatite/Clinoptilolite/NH2 Adsorbent for Simultaneous Removal of Cr (VI) and F, *Silicon*, 2022, **1–17**, 8643–8659.

73 A. Sadeghizadeh, F. Ebrahimi, M. Heydari, M. Tahmasebikohyani, F. Ebrahimi and A. Sadeghizadeh, Adsorptive removal of Pb (II) by means of hydroxyapatite/chitosan nanocomposite hybrid nanoadsorbent: ANFIS modeling and experimental study, *J. Environ. Manage.*, 2019, **232**, 342–353.

74 N. A. Abdelwahab, N. S. Ammar and H. S. Ibrahim, Graft copolymerization of cellulose acetate for removal and recovery of lead ions from wastewater, *Int. J. Biol. Macromol.*, 2015, **79**, 913–922.

75 X. Yang, N. Guo, Y. Yu, H. Li, H. Xia and H. Yu, Synthesis of magnetic graphene oxide-titanate composites for efficient removal of Pb (II) from wastewater: performance and mechanism, *J. Environ. Manage.*, 2020, **256**, 109943.

76 P. Khorshidi, R. H. S. M. Shirazi, M. Miralinaghi, E. Moniri and S. Saadi, Adsorptive removal of mercury (II), copper (II), and lead (II) ions from aqueous solutions using glutathione-functionalized NiFe2O4/graphene oxide composite, *Res. Chem. Intermed.*, 2020, **46**(7), 3607–3627.

77 K. Vijayalakshmi, B. M. Devi, S. Latha, T. Gomathi, P. N. Sudha, J. Venkatesan, *et al.*, Batch adsorption and desorption studies on the removal of lead (II) from aqueous solution using nanochitosan/sodium alginate/microcrystalline cellulose beads, *Int. J. Biol. Macromol.*, 2017, **104**, 1483–1494.

78 R. G. Huamani-Palomino, C. R. Jacinto, H. Alarcón, I. M. Mejía, R. C. López, D. de Oliveira Silva, *et al.*, Chemical modification of alginate with cysteine and its application for the removal of Pb (II) from aqueous solutions, *Int. J. Biol. Macromol.*, 2019, **129**, 1056–1068.

79 J. Shang, Y. Guo, D. He, W. Qu, Y. Tang, L. Zhou, *et al.*, A novel graphene oxide-dicationic ionic liquid composite for Cr (VI) adsorption from aqueous solutions, *J. Hazard. Mater.*, 2021, **416**, 125706.

80 P. C. Bandara, J. Peña-Bahamonde and D. F. Rodrigues, Redox mechanisms of conversion of Cr (VI) to Cr (III) by graphene oxide-polymer composite, *Sci. Rep.*, 2020, **10**(1), 1–8.

81 Y. X. Ma, W. J. Shao, W. Sun, Y. L. Kou, X. Li and H. P. Yang, One-step fabrication of β-cyclodextrin modified magnetic graphene oxide nanohybrids for adsorption of Pb (II), Cu (II) and methylene blue in aqueous solutions, *Appl. Surf. Sci.*, 2018, **459**, 544–553.

82 Q. Lian, Z. U. Ahmad, D. D. Gang, M. E. Zappi, D. L. B. Fortela and R. Hernandez, The effects of carbon disulfide driven functionalization on graphene oxide for enhanced Pb (II) adsorption: Investigation of adsorption mechanism, *Chemosphere*, 2020, **248**, 126078.

83 V. P. Chauke, A. Maity and A. Chetty, High-performance towards removal of toxic hexavalent chromium from aqueous solution using graphene oxide-alpha cyclodextrin-polypyrrole nanocomposites, *J. Mol. Liq.*, 2015, **211**, 71–77.

84 Z. Wang, W. Xu, F. Jie, Z. Zhao, K. Zhou and H. Liu, The selective adsorption performance and mechanism of multiwall magnetic carbon nanotubes for heavy metals in wastewater, *Sci. Rep.*, 2021, **11**(1), 16878.

85 J. M. Brady and J. M. Tobin, Binding of hard and soft metal ions to Rhizopus arrhizus biomass, *Enzyme Microb. Technol.*, 1995 Sep 1, **17**(9), 791–796.

86 P. Karthikeyan, S. S. D. Elanchezhiyan, H. A. T. Banu, M. H. Farzana and C. M. Park, Hydrothermal synthesis of hydroxyapatite-reduced graphene oxide (1D–2D) hybrids with enhanced selective adsorption properties for methyl orange and hexavalent chromium from aqueous solutions, *Chemosphere*, 2021, **276**, 130200.

87 M. S. Samuel, J. Bhattacharya, S. Raj, N. Santhanam, H. Singh and N. P. Singh, Efficient removal of Chromium (VI) from aqueous solution using chitosan grafted graphene oxide (CS-GO) nanocomposite, *Int. J. Biol. Macromol.*, 2019, **121**, 285–292.

88 H. H. Najafabadi, M. Irani, L. R. Rad, A. H. Haratameh and I. Haririan, Removal of Cu 2+ , Pb 2+ and Cr 6+ from aqueous solutions using a chitosan/graphene oxide composite nanofibrous adsorbent, *RSC Adv.*, 2015, **5**(21), 16532–16539.

89 Y. Zhou, W. Li, X. Jiang, Y. Sun, H. Yang, Q. Liu, *et al.*, Synthesis of strontium (Sr) doped hydroxyapatite (HAp) nanorods for enhanced adsorption of Cr (VI) ions from wastewater, *Ceram. Int.*, 2021, **47**(12), 16730–16736.

90 M. G. Azam, M. H. Kabir, M. A. A. Shaikh, S. Ahmed, M. Mahmud and S. Yasmin, A rapid and efficient adsorptive removal of lead from water using graphene oxide prepared from waste dry cell battery, *J. Water Proc. Eng.*, 2022, **46**, 102597.

91 A. M. Mohammad, T. A. S. Eldin, M. A. Hassan and B. E. El-Anadouli, Efficient treatment of lead-containing wastewater by hydroxyapatite/chitosan nanostructures, *Arabian J. Chem.*, 2017, **10**(5), 683–690.

92 L. Cui, Y. Wang, L. Gao, L. Hu, L. Yan, Q. Wei, *et al.*, EDTA functionalized magnetic graphene oxide for removal of Pb (II), Hg (II) and Cu (II) in water treatment: adsorption mechanism and separation property, *Chem. Eng. J.*, 2015, **281**, 1–10.